THIS MANUSCRIPT HAS BEEN SUBMITTED TO THE JOURNAL OF GLACIOLOGY AND HAS NOT BEEN PEER-REVIEWED.

Steady crevasse locations in Pâkitsoq, Greenland over one decade: Results from MimiNet, a new deep-learning model for crevasse detection

Journal:	*Journal of Glaciology*
Manuscript ID	JOG-2025-0095.R3
Manuscript Type:	Article
Date Submitted by the Author:	n/a
Complete List of Authors:	Khan, Naureen; University at Buffalo, Geology Poinar, Kristin; University at Buffalo, Earth Sciences Briner, Jason; University at Buffalo, Geology Crooks Nowicki, Sophie; University at Buffalo, Geology Mejia, Jessica; Syracuse University, Department of Earth and Environmental Sciences Avellaneda, Alexandra; University at Buffalo Verné, Mary; University at Buffalo, Geology
Keywords:	Crevasses, Remote sensing, Glacier hydrology
Abstract:	If crevasse fields deliver meltwater to the bed of the Greenland Ice Sheet, it would affect seasonal ice flow speeds and total mass balance. The best current automated tool to map crevasse fields extends only a few dozen kilometers inland. To address this gap, we develop MimiNet, a neural-network-based tool that identifies surface crevasse fields. We train MimiNet on Sentinel-1 scenes across a 629 km^2 area in Pâkitsoq, central-western Greenland, and use it to locate crevasse fields annually over 2015–2024. We find that the crevassed area varied from a minimum of 106±5 km^2 in 2019 to a maximum of 144±6 km^2 in 2016, with no overall trend over the ten-year study period. We find some evidence that seasonal ice velocity anomalies in crevasse fields are higher than those in moulin-drained areas in the late melt season. This may suggest that the

	subglacial drainage system under crevasse fields remains inefficient all summer, and thus that at least some Pâkitsoq crevasse fields deliver meltwater to the bed. Interannual variability in ice dynamics may drive the observed variability in crevassed areas; we expect crevasse extent to become more variable in time as ice flow speeds, and their variations, amplify under climate change.

SCHOLARONE MANUSCRIPTS

Steady crevasse location in Pâkitsoq, Greenland over one decade: Results from MimiNet, a new deep-learning model for crevasse detection

Naureen Khan[1], Kristin Poinar[1,2], Jason Briner[1], Sophie Nowicki[1,2], Jessica Mejia[1,3], Alexandra Avellaneda[1] and Mary Verné[1]

University at Buffalo, NY, Department of Earth Sciences[1], RENEW Institute[2], Syracuse University, NY, Department of Earth and Environmental Sciences[3]

Abstract

If crevasse fields deliver meltwater to the bed of the Greenland Ice Sheet, it would affect seasonal ice flow speeds and total mass balance. The best current automated tool to map crevasse fields extends only a few dozen kilometers inland. To address this gap, we develop MimiNet, a neural-network-based tool that identifies surface crevasse fields. We train MimiNet on Sentinel-1 scenes across a 629 km^2 area in Pâkitsoq, central-western Greenland, and use it to locate crevasse fields annually over 2015–2024. We find that the crevassed area varied from a minimum of 106±5 km^2 in 2019 to a maximum of 144±6 km^2 in 2016, with no overall trend over the ten-year study period. We find some evidence that seasonal ice velocity anomalies in crevasse fields are higher than those in moulin-drained areas in the late melt season. This may suggest that the subglacial drainage system under crevasse fields remains inefficient all summer, and thus that at least some Pâkitsoq crevasse fields deliver meltwater to the bed. Interannual variability in ice dynamics may drive the observed variability in crevassed areas; we expect crevasse extent to become more variable in time as ice flow speeds, and their variations, amplify under climate change.

For Peer Review

1 Introduction

1.1 Surficial meltwater routing on the Greenland Ice Sheet

Between 1992 – 2020, the Greenland Ice Sheet has contributed 14 mm to global mean sea level rise, an average of 4.7 mm per decade (Otosaka and others, 2022). This mass loss has primarily occurred through ice discharge (calving) and surface meltwater runoff (Van Den Broeke and others, 2016). Runoff produced in the ice sheet ablation zone flows downslope in supraglacial streams and rivers, with some 80% of the runoff at elevations >~1000 meters flowing directly to the bed via moulins (Smith and others, 2015). The fate of the remaining 20% is less studied, and includes supraglacial storage in wet snow and lakes, or delivery to surface crevasses (Smith and others, 2015). Study of moulins has outpaced that of crevasses in recent years (e.g., Smith and others, 2017); it is not yet known whether crevasses deliver the melt to the bed or store it englacially to slowly refreeze (Poinar, 2015).

Surface crevasses are fractures that form from deviatoric stresses as ice flows over an irregular bed, through a constriction, or responds to surge flow (Colgan and others, 2016; Zheng and others, 2019; Reynolds and others, 2025). Meltwater can drive the deepening of crevasses through hydrofracture; if there is sufficient water volume, crevasses can fracture hundreds of meters or more down to the ice-sheet bed (Das and others, 2008; Krawczynski and others, 2009). These crevasses can then maintain a direct hydraulic connection for meltwater from the ice sheet surface to the ice sheet bed (Hooke, 1989). Consistent meltwater input through these fully-propagated crevasses can form moulins, which are near-vertical tunnel-like features that carry meltwater to the basal environment (Alley and others, 2005; Das and others, 2008).

Once in the basal environment, surface meltwater can affect the state of the subglacial drainage system (Bartholomew and others, 2010; Van de Wal and others, 2015; Nienow and others, 2017). During the early part of the melt season, surface meltwater inputs increase the water pressure in the subglacial system, increasing basal lubrication that speeds basal sliding velocities (Bartholomew and others, 2010). Later in the melt season, sustained meltwater inputs can develop a channelized or efficient subglacial drainage system (Flowers, 2014). This decreases the overall water pressure and slows basal sliding velocities, allowing additional meltwater to enter the subglacial system without exceeding the hydraulic capacity of the channels or increasing sliding velocities (Schoof, 2010; Banwell and others, 2016). Thus, surface meltwater input locations are important drivers of the spatial organization of subglacial channelization (Gulley and others, 2012; Mejia and others, 2022).

In order for a crevasse to deliver surface meltwater to the bed, conditions on the stress environment and meltwater supply must be met (e.g., Krawczynski and others, 2009; Alley and others, 2005, McGrath and others, 2011). These conditions vary regionally across the ice sheet, and investigations of various regions and techniques (field-based, model-based, or both) have found different answers to this question. When crevasses lack meltwater input, crevasses typically propagate only tens of meters deep (Nye, 1955). Field-informed studies from Pâkitsoq, central western Greenland suggest that crevasses there transport supraglacial meltwater several hundred meters deep into the englacial system, where it can persist for decades before eventually refreezing and warming the surrounding ice by several degrees (Phillips and others, 2010; Luthi and others, 2015, Poinar and others, 2016). On the other hand, McGrath and others (2011) found that crevasse fields drain about 48% of the surface meltwater runoff to the bed, but the precise fraction may vary across different crevasses, crevasse fields, regions, or across seasons. Similarly, Koziol and others (2017) found that 47% of the surface meltwater runoff in Pâkitsoq is drained through crevasses. The body of observations suggests that crevasses serve as drainage pathways for meltwater to exit the supraglacial drainage system but whether they carry that water to the bed or retain it englacially is not generally known.

As surface velocity patterns vary over time, it will change the spatial distribution of crevasses (Koziol and Arnold, 2018) and their role in delivering meltwater to the bed. Colgan and others (2011) found a substantial expansion of crevassed area extent in Pâkitsoq between 1985 and

For Peer Review

2009, while more recently, Chudley and others (2025) found the opposite: that crevassed area reduced between 2016 and 2021 in central western Greenland. This suggests that there are substantial changes in the crevassing dynamics from decade to decade, but the year-to-year spatial evolution in the crevassed area of Pâkitsoq is not yet known.

Here we develop an automated method to detect crevasse fields from satellite imagery and apply it to Pâkitsoq, central western Greenland, over 2015–2024, in order to measure the trend and interannual variability in the crevassed area extent. We also analyze the seasonal evolution of ice flow velocity across crevassed and moulin-drained areas to test the hypothesis that crevasses in Pâkitsoq carry meltwater to the bed, versus storing it englacially without delivering it to the bed. During the peak melt season, if meltwater reaches the bed through crevasses, its addition to the basal hydrologic system should locally reduce the effective pressure of the ice sheet, increasing ice flow speeds (Nienow and others, 2017).

2. Background

2.1 Existing methods for crevasse detection

The study of crevasses on ice sheets has a long history. For many decades, field crews have performed crevasse detection on ice sheets for the safety of ground-based research teams (Cook, 1956; Pings, 1961; Taurisano and others, 2006; Eder and others, 2008). Ground penetrating radar (GPR) is the most common on-site method. The radar waves can penetrate through the snow and ice layers to several tens to thousands of meters depth, depending on wavelength (Eder and others, 2008). Previous studies have collected and analyzed GPR data at study areas across a range of scales, including 1.8 km^2 (Ravanel and others, 2022), 3 km^2 (Kaluzienski and others, 2019), and 25 km^2 (Walker and others, 2019). Using GPR carried by helicopter, Thompson and others (2020) surveyed a 296 km^2 area. Assessing areas larger than this, however, requires a remote-sensing approach. Remote sensing allows features indicative of crevasses to be detected across wide areas, facilitating larger-scale hazard mapping (Colgan and others, 2011; Koike and others, 2012; Chudley and others, 2021; Herzfeld and others, 2021; Marsh and others, 2021; Libert and others, 2022). To date, these indicative features have included straight lines in visible imagery, bright places in radar imagery, or trenches in DEMs (Colgan and others, 2011; Marsh and others, 2021; Chudley and others, 2021; Van Wyk de Vries and others, 2023; Chudley and others, 2025) that have been detected manually by individual users, or algorithmically in an automated way. Manual analysis of remote sensing data (e.g., Colgan and others, 2011; Hoffman and others, 2018) is a time-consuming endeavor.

Automated analyses of remote sensing imagery offer significant advantages. Recently, deep learning techniques have evolved, which enable data analysis over very large spatial scales, enabling a comprehensive dataset of crevasse distribution and ice sheet dynamics across the entire Antarctic Ice Sheet (Lai and others, 2020, Zhao and others, 2022, Surawy-Stepney and others, 2023). However, applying deep learning to detect crevasses from remote sensing imagery

For Peer Review

over the Greenland Ice Sheet has not yet been done. This is in part because of the difficulty of differentiating crevasses from other surface features, such as meltwater streams and lakes, which are prevalent in the Greenland ablation zone but rare across most of Antarctica. These distractor features are similar in scale (widths on the order of meters) to Greenland crevasses, which are substantially smaller and thus more difficult to resolve than Antarctic fractures (widths on the order of hundreds of meters). This work aims to address this challenge by developing an automated crevasse detection method for the Greenland Ice Sheet using remote sensing over a 629 km^2 area of Pâkitsoq (Fig. 1a), a historically well-studied region in central western Greenland.

2.2 Crevasse detection using Sentinel-1 SAR imagery

The Sentinel-1 satellite constellation carries Synthetic Aperture Radar (SAR) instruments that transmit C-band microwaves at 5.3 GHz frequency toward a surface, then receive back the reflected microwave signal (European Space Agency, 2014). In areas where the ice surface is smooth, SAR microwaves reflect a small portion of the microwave energy back to the receiver, making the surface appear dark in the produced image. Where the surface is rough, backscatter is higher, making the terrain appear brighter. SAR data thus provides a clear contrast between crevasse fields and non-crevassed ice, as rough crevasse fields appear bright and smooth ice surfaces appear dark in SAR imagery. The spatial resolution of Sentinel-1 SAR imagery is 10 meters, which is larger than the typical width of an individual crevasse (~2 meters). A pixel that overlaps a crevasse should therefore appear somewhat brighter than its surroundings, although not as bright as if a crevasse occupied the entirety of the pixel. However, due to the long length of most crevasses (at least a few hundred meters, shown in Fig. 1b–c), a single crevasse appears in Sentinel-1 SAR as a continuous line of brighter-than-average pixels. Furthermore, crevasses often cluster together in crevasse fields, which appear as bright patches with a distinct linear pattern (Fig. 1c).

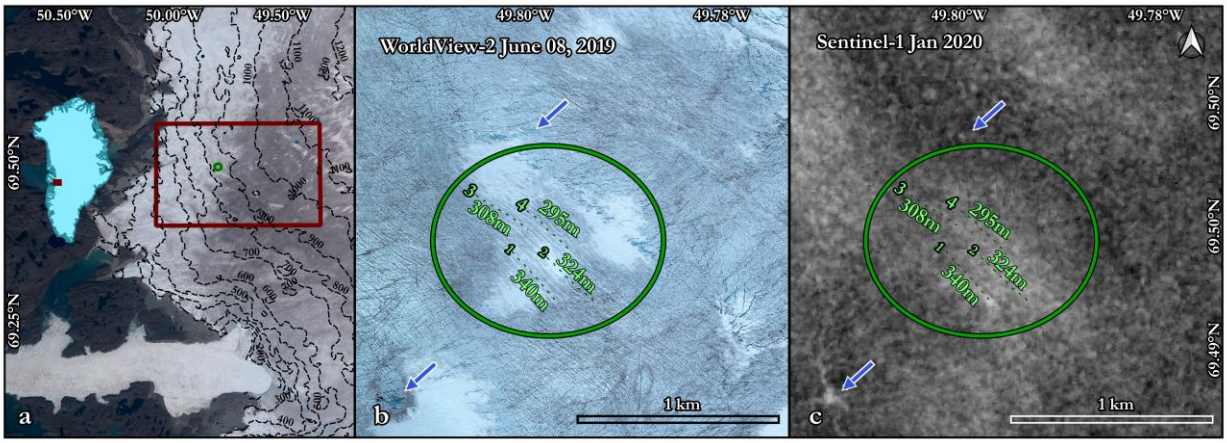

Figure 1: a) Sentinel-2 RGB image from August 2019 median showing our 629 km^2 study area of Pâkitsoq, central-western Greenland, within the red box, overlaid by 100m surface elevation contours from BedMachine v5. Green circle shows the crevasse field in panels b and c. b) WorldView-2 imagery

acquired June 08, 2019 (2.2 km × 2.2 km) showing a crevasse field in green circle. Green dashed lines denote four specific crevasses visible in this crevasse field, labeled with their corresponding lengths. Blue arrows indicate supraglacial drainage features near this crevasse field. c) Median of all Sentinel-1 SAR Level-1 Ground Range Detected HH single co-polarization scenes acquired in January 2020 (2.2 km × 2.2 km) showing the same crevasse field visible as a bright patch (green circle) with the four individual crevasses (green lines) discernible as thin linear features. Blue arrows again mark the two water features which appear as bright non-linear features.

Alternative remote-sensing data sources that resolve crevasses include optical image data from the European Space Agency's Sentinel-2 satellite constellation (10-meter multispectral spatial resolution), commercial WorldView-1 and WorldView-2 satellites (0.5-meter panchromatic and 2-meter multispectral spatial resolution, respectively), and NASA / USGS's Landsat-8/9 satellite constellation (15-meter panchromatic and 30-meter multispectral spatial resolution). In all of these sources, even in the highest-resolution WorldView-1 data, some crevasses and crevasse fields are not visible due to snow cover, cloud cover or daylight conditions. These problems are not faced by Sentinel-1, whose C-band SAR can penetrate the dry snowpack to a maximum depth of ~9 meters, and typically a few meters in our study area (Rignot and others, 2001). This makes Sentinel-1 imagery a very suitable dataset for detecting crevasses. One limitation, however, of polar-orbiting satellites is that these may miss crevasse fields that are oriented unfavorably to look direction (Hoffman and others, 2025). For instance, some features may be visible only in ascending orbits, others only in descending orbits, and other features not in either (Hoffman and others, 2025)

Crevasses at a perpendicular direction to the SAR incidence angle scatter back higher energy off the crevasse edge or wall facing the sensor, producing a bright surface return (Fig. 2). On the other hand, crevasses encountered at a parallel direction do not face the backscatter-enhancing wall and thus undergo higher forward scattering, producing a darker surface return (Marsh and others, 2021).

For Peer Review

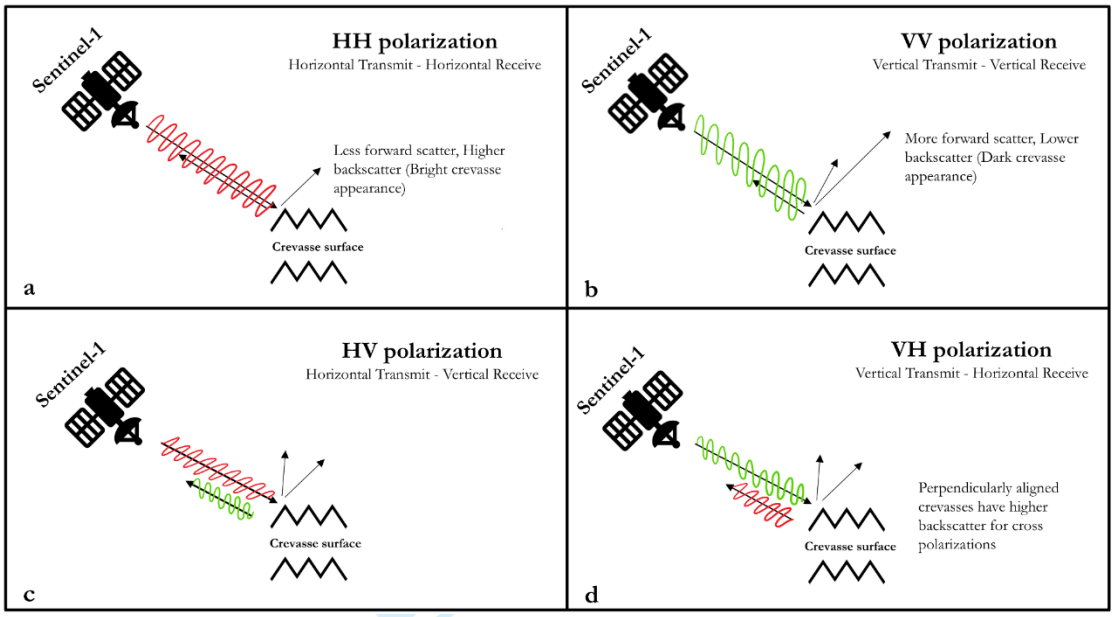

Figure 2: Sentinel-1 SAR polarization on crevasse surface: a) HH single co-polarization mode transmits and receives horizontally polarized microwaves. The HH mode is sensitive to surface slope, so crevasses create high backscatter and low forward scatter, producing a bright return in crevassed areas. b) VV single co-polarization mode transmits and receives vertically polarized microwaves. The VV mode is sensitive to surface roughness, so crevasses cause low backscatter and high forward scatter. This creates dark returns in crevassed areas. c and d) HV and VH cross-polarization modes combine some of the features of the co-polarization (HH and VV) modes, sometimes producing bright returns in crevassed areas but generally returning lower energy overall. The cross-polarization modes produce contrast between crevassed and non-crevassed areas but suffer from higher energy loss.

Sentinel-1 SAR has four polarization modes: Horizontal Transmit and Horizontal Receive (HH) and Vertical Transmit and Vertical Receive (VV) single co-polarization, Horizontal Transmit and Vertical Receive (HV) and Vertical Transmit and Horizontal Receive (VH) dual band cross-polarization. Figure 2 illustrates the differences in backscatter among these modes. HH single co-polarization mode transmits and receives microwaves in the horizontal direction; when the transmit/receive orientation is perpendicular to the crevasse strike, the crevasse walls reflect back high scatter and consequently produce low forward-scatter. VV single co-polarization mode transmits and receives microwaves in the vertical direction. The vertically polarized waves are sensitive to surface roughness in any direction, so crevassed surfaces, regardless of their strike, produce high forward-scatter, in contrast to smooth surfaces that reflect higher scatter. This makes crevasses appear dark and smooth surfaces appear bright in VV polarization. Finally, HV and VH dual band cross-polarization modes each use both the horizontal and vertical directions. The vertical portion of HV and VH polarization produces forward-scattering or double-bounce backscattering on crevasses, which makes them appear dark, while smooth surfaces appear bright. Both HV and VH polarization modes yield high contrast between crevassed and non-crevassed areas (Marsh and others, 2021). However, the cross-polarization modes produce lower backscatter overall compared to the like-polarization

For Peer Review

modes, making dimmer images that have an overall less separable signal between crevassed and smooth areas. Therefore, we judge the HH single co-polarization SAR mode to work best for crevasse field detection in our application because it tends to generate bright observations with good contrast between crevasse fields and uncrevassed ice, and because it reduces noise when a double bounce backscattering occurs.

SAR backscatter from the Sentinel-1 satellite is sensitive to the presence of water in ice and snow. Thus, during the melt season when the surface is wet, water will absorb some microwave radiation, making the ice-sheet surface appear darker in the SAR imagery than at other times of year (Marin and others, 2020). This makes crevasse detection using SAR imagery more difficult, as there are lower returns from all surfaces, including crevassed areas. Therefore, we judge that January through April, when the surface is dry and therefore has low absorption of microwave radiation, are optimal for detecting crevasse fields.

2.3 Crevasse detection using deep learning

Deep learning models comprise multiple layers of neural networks that extract information from input data. We use a semantic segmentation-based convolutional neural network (CNN), which detects features from input images using supervised classification (LeCun and others, 2015). Supervised classification requires that each input image be labeled or classified; the CNN ingests the labels to learn patterns inherent in the target features (Long and others, 2015). CNNs comprise interconnected nodes that are arranged in layers. Each node takes in inputs, processes them, and produces an output that it sends to the next layer of nodes (Buduma and others, 2022). The CNN assigns weights to the connections between the nodes, then modifies these weights during the training process to enhance the performance of the network against the known labels (Alzubaidi and others, 2021). Most image-processing CNNs are equipped with multiple convolution filters by which the models detect the target class from all features obtained through convolution (Gu and others, 2018). These convolution filters are small matrices that convolve across the image to find natural edges, lineations, or feature boundaries in the image (Zeiler and others, 2014).

Recent studies have harnessed the potential of CNN-based deep learning to identify fractures on ice sheets in Antarctica (Lai and others, 2020; Zhao and others, 2022; Suraway-Stepney and others, 2023). However, no study yet has used CNNs for the identification of Greenland crevasses. The closest study is Chudley and others (2021), who applied a random forest classifier to elevation data over a small (7 km^2) field study area in western Greenland. Random forest classifiers excel at classifying features of pre-identified types, for example healed crevasses, narrow crevasses, and wide or water-filled crevasses (Chudley and others, 2021); however, they are less able to broaden the detections into, for instance, a general “crevasse” type. For this capability, CNNs are optimal.

We use a CNN-based deep learning algorithm to extract patterns from Sentinel-1 SAR satellite imagery to detect crevasses at a regional scale. We use a modified version of the U-Net deep

For Peer Review

learning architecture with fully connected convolutional filters (Ronneberger and others, 2015). U-Net improves upon the base CNN algorithm by upsampling the extracted features into the same (or similar) pixel resolution and orientation as the original input image. Thus, the U-Net model not only detects target features in an image but also identifies their spatial locations. U-Net is designed to locate specific user-defined classes within an image by analyzing the image at multiple different scales. U-Net has been previously used for detecting glacier calving fronts in Greenland (Baumhoer and others, 2019; Mohajerani and others, 2019; Cheng and others, 2021). It has also been implemented for detecting fractures on Antarctic ice shelves (Lai and others, 2020; Zhao and others, 2022; Surawy-Stepney and others, 2023). For example, Surawy-Stepney and others (2023) used a shallow layered U-Net to detect large (~200-meter width) fractures on ice shelves and smaller (~50-meter width) fractures on grounded ice; the latter is similar to a small crevasse field in Greenland. Their results suggest that small crevasses are significantly more difficult to identify than large crevasses. We address this challenge by developing a new model based on U-Net to detect densely spaced, narrow crevasses on the Greenland Ice Sheet.

3 Methods

3.1 Study area and remote sensing data

Our study area encompasses a ~30 × 20 km^2 area of the Pâkitsoq region in central western Greenland, centered at 69.47°N, 49.72°W. This region has a long history of glaciological studies (Thomsen and others, 1989; Colgan and others, 2011; Andrews and others, 2014; Luthi and others, 2015; Koziol and others, 2017; Mejia and others, 2022). Particularly, Hoffman and others (2018) used WorldView-2 satellite imagery to manually digitize the locations of crevasse fields in a subset of our study area over 2009–2011, making a valuable independent comparison dataset.

For Peer Review

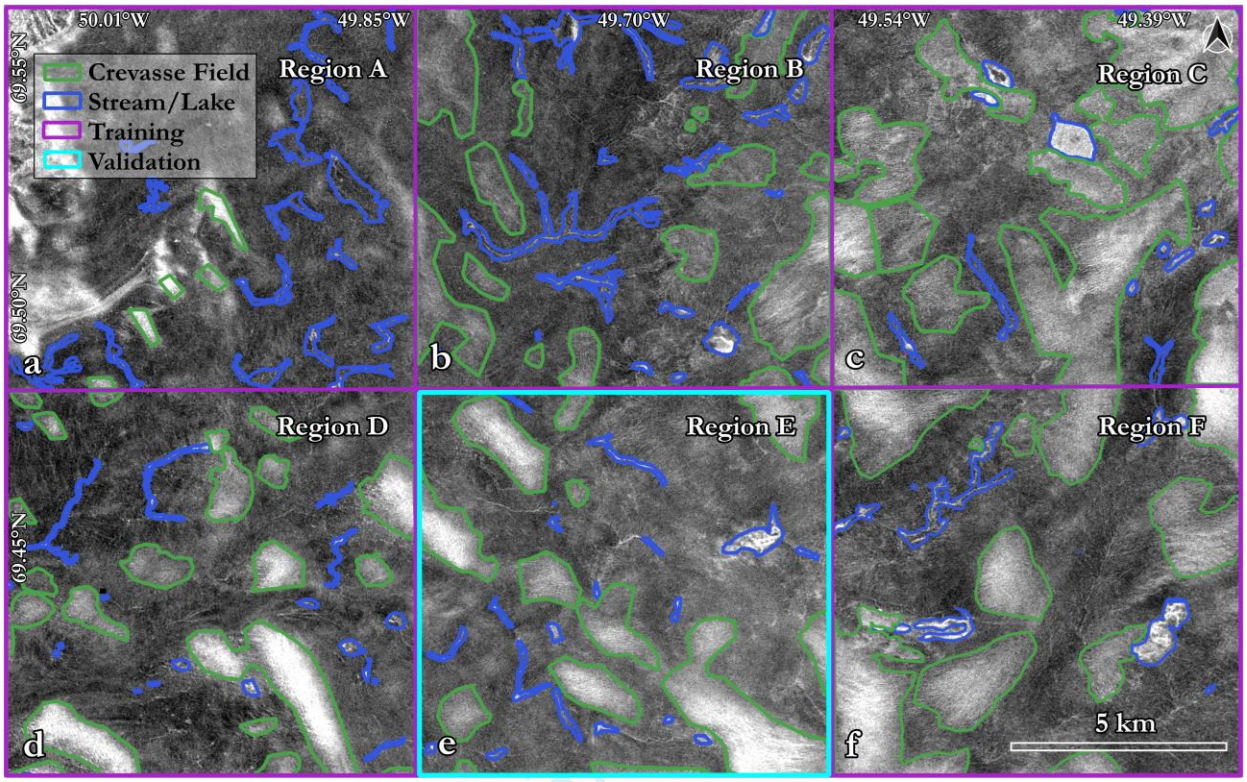

Figure 3: Study area, a 30.72 km × 20.48 km area of Pâkitsoq shown in Fig. 1a. We divide this area into regions A–F. Region A shows 15m ice sheet margin black outlines from GIMP ice mask. We use the median of all Sentinel-1 SAR Level-1 GRD HH single co-polarization scenes acquired in January 2020 for training the model. Manually digitized ground truth labels containing crevasse field (green polygons) and remnant stream/lake (blue polygons) are used as training (purple boxes) and validation (cyan box) datasets.

We constructed and analyzed a representative wintertime median scene from Sentinel-1 SAR Level-1 Ground Range Detected (GRD) imagery covering 30.72 km × 20.48 km in Pâkitsoq. We constructed this scene from five individual Sentinel-1 scenes, acquired on January 1, 7, 13, 19, and 25 of 2020, which we accessed using Google Earth Engine (Gorelick and others, 2017). Google Earth Engine pre-processes Sentinel-1 SAR raw scenes using the Sentinel-1 Toolbox, which applies thermal noise removal, radiometric calibration to convert radar backscatter coefficient in decibels using log-scaling for normalization, and terrain correction to orthorectify the scenes (Veci and others, 2017). We selected the HH single co-polarization, interferometric swath mode, and ascending orbit, generated their pixel-by-pixel median over the five acquisition dates, and exported the resultant median scene as a 64-bit GeoTiff raster with the native 10-meter spatial resolution. Because of relatively slow ice speeds in our study area (~100 m/yr), this temporal median method introduces only a low amount of feature blurring. Across the 25 days of January we use, the ice moved ~8 meters, or 1 pixel. Across four months of spring (January through April), the movement is ~33 meters, or 3 pixels. This keeps the crevasse fields, which are hundreds to thousands of meters wide, intact, while producing some blurry effects by tens of

For Peer Review

meters around the edges of crevasse fields. This was the best way we tested that could reduce speckle noise enough to make the deep learning model perform well (Section S1).

We divided our study area into six regions, each 10.24 km × 10.24 km (Fig. 3) and allocated them as training and testing (regions A, B, C, D, and F) and validation (region E) datasets. We next subdivided each region raster into four tiles (5.12 km × 5.12 km each) to reduce computational runtime and maintain compatibility with U-Net, which expects 512 × 512 pixel inputs. Thus, six regions divided into four tiles yielded 24 tiles each of 512 × 512 pixels; we used 20 tiles as the training and testing data and 4 tiles as the validation data. We chose region E to be the validation dataset as it has a mix of crevasse fields, supraglacial streams, and lakes. The validation dataset consisted of Sentinel-1 median scenes of January 2018, 2019, and 2020 (Table S2) to increase the variability in surface conditions

For Peer Review

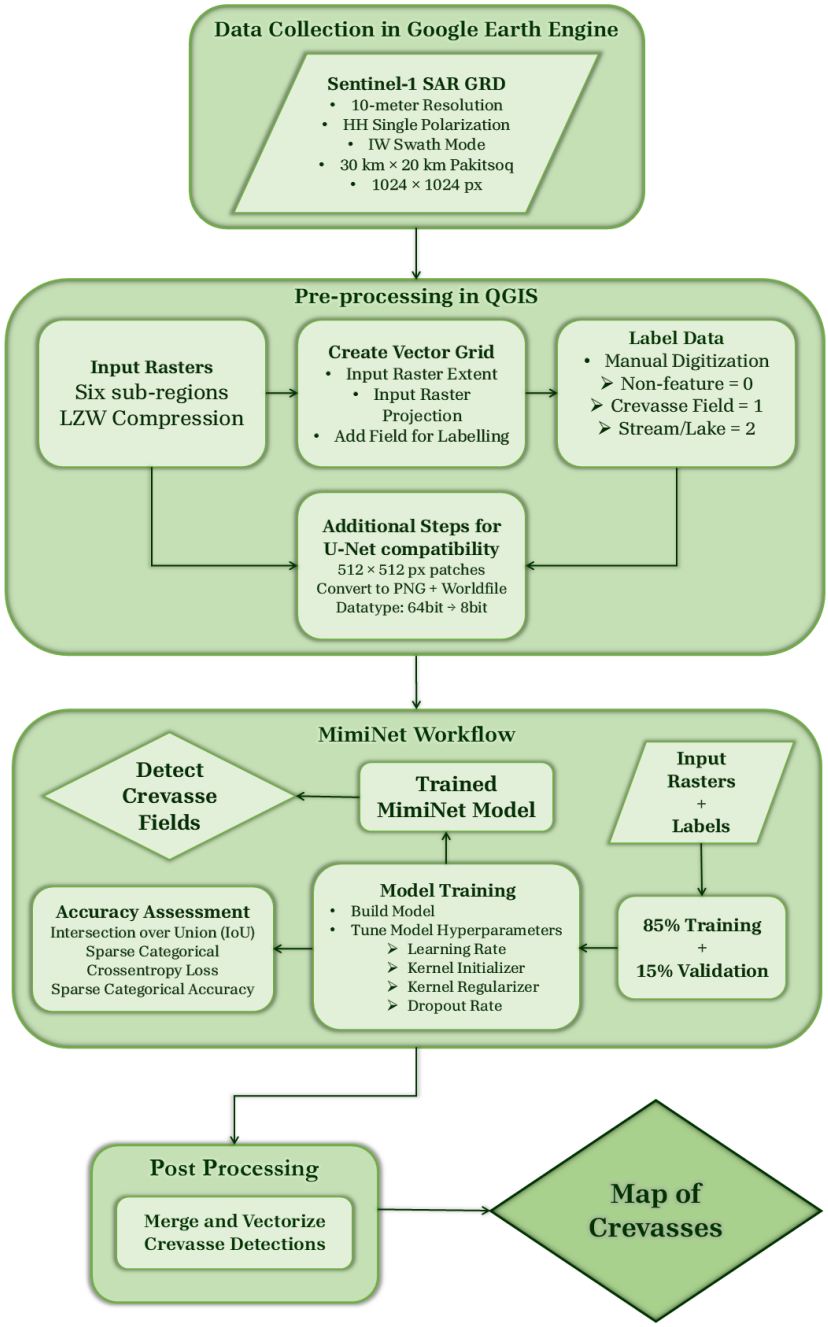

287

288 *Figure 4: Automated crevasse detection workflow. From the top down: Data collection in Google Earth*
289 *Engine: export Sentinel-1 SAR imagery for Pâkitsoq region with outlined parameters → Pre-processing in*
290 *QGIS: change format of the exported rasters + ground truth labels → MimiNet workflow: input processed*
291 *images and labels to train model + perform model hyperparameter tuning = Crevasse detection + metric*
292 *scores → Post-processing: merge and vectorize all crevasse field detections → Final output of map of*
293 *crevasse fields.*

294 3.2 MimiNet crevasse field detection

We developed MimiNet, a deep learning workflow that adapts U-Net to the specific problem of crevasse field detection on the Greenland Ice Sheet ablation area from Sentinel-1 SAR images. Like U-Net, MimiNet uses image segmentation, which is a pixel-based classification method that requires ground truth labels that identify target features in the training dataset. The primary target feature of MimiNet is crevasse fields, but these features are interspersed with the remnants of summertime meltwater features, such as supraglacial streams and supraglacial lake beds, which often appear similarly bright in Sentinel-1 SAR imagery (Surdu and others, 2014). To avoid conflating crevasse fields with these remnant meltwater features, we trained the model to identify three classes: non-features (ice without crevasses or streams), crevasse fields, and remnant supraglacial streams/lakes. We manually created labels by outlining all features in the median of all Sentinel-1 scenes acquired over January 2020 across our study area (Section 3.1), using a map scale of 1:20000 and a digitization radius of 150–600 m (15–60 pixels in Sentinel-1 imagery) in QGIS. Labels for Region E in January 2018 and 2019 median scenes were generated by a different individual to strengthen the model training process. Figure 5 shows the processing chain: the input raster, the manually annotated vector shapefile, and finally the three categories of rasterized labels. Our three target classes are as follows: non-features (white regions), crevasse fields (green regions), and remnant stream/lake (blue regions).

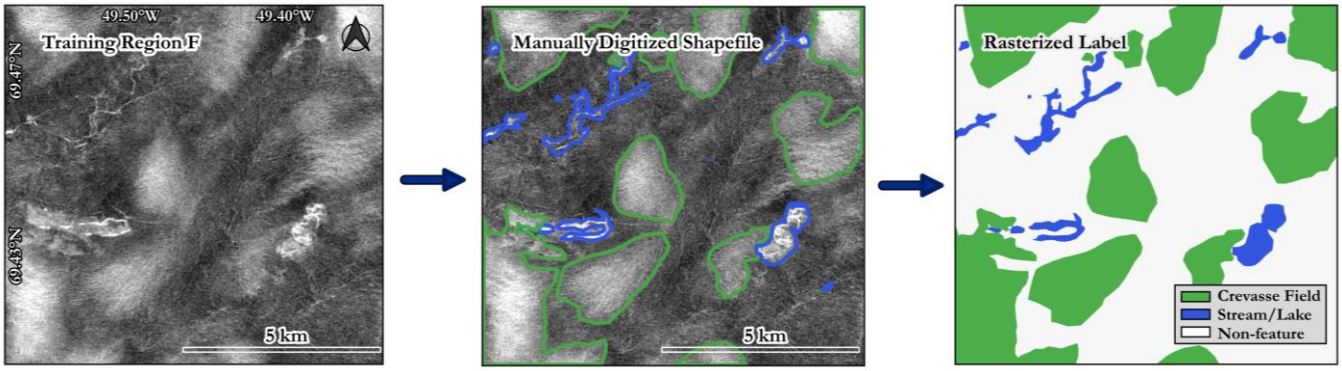

Figure 5: (From left to right) The median of all Sentinel-1 SAR Level-1 GRD HH single co-polarization scenes acquired in January 2020 over the training region F (1024 px × 1024 px) ⇒ Manually classified vector shapefile containing crevasse fields (green polygons) and remnant stream/lake (blue polygons) ⇒ Rasterized labels containing three classes: non-features (class 0, white region), crevasse fields (class 1, green regions), and remnant stream/lake (class 2, blue regions).

3.2.1 MimiNet model structure

We adapted the U-shaped U-Net Architecture to develop MimiNet, as shown in Figure 6. The left portion of Figure 6 shows the downsampling path and the right portion shows the upsampling path. MimiNet extracts features through three layers in the downsampling path. The inputs are 512 × 512 pixel single-band 8-bit images with pixel values from 0–255. To gain compatibility with U-Net, we converted both the raster (Fig. 3) and ground truth labels (Fig. 5) to 8-bit images using the LZW Lossless Image Compression method in QGIS. In each layer, the image is processed through two 3 × 3 convolution filters and then one 2 × 2 max pooling filter.

Each convolution filter (yellow arrow) convolves across the image to extract feature maps. In the first layer, the two convolution operations produce 16 extracted feature maps per image. In the second layer, the two convolution operators extract 32 feature maps, and 64 feature maps in the third layer. At the end of each layer along the downsampling path, a max pooling operator (pink arrow) takes the maximum pixel values across 2 × 2 windows, thereby reducing the spatial size by a factor of four (a factor of two in each direction), i.e, from 512 × 512 to 256 × 256 in the second layer, and from 256 × 256 to 128 × 128 in the third layer. Next, the 64 feature maps extracted at the third layer are upsampled to regain the spatial size lost along the downsampling path. A 2 × 2 upsampling filter (purple arrow) duplicates rows and columns of the image matrix, then the feature maps are cropped and concatenated with the feature maps from each downsampling layer. Two more 3 × 3 convolution filters are applied after every upsampling and then a final 1 × 1 convolution filter (also known as the activation function) is applied to reduce the image depth from 16 feature maps to the number of target classes (three), producing a 512 × 512 × 3 output image.

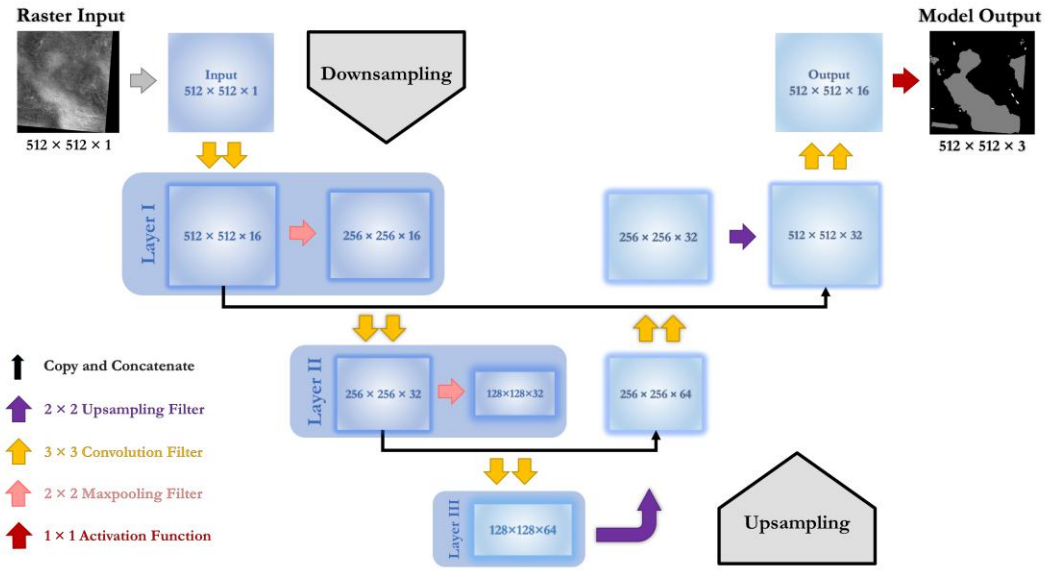

Figure 6: MimiNet model structure for detecting crevasses on the Greenland Ice Sheet. The downsampling and upsampling design its U-shaped architecture. Different arrows indicate the filters used in the model. The raster input is 512 pixels × 512 pixels from the median of all Sentinel-1 SAR Level-1 GRD HH single co-polarization scenes acquired in January 2020 (top-left) and the model output (top-right) contains detected crevasse fields (gray regions), remnant supraglacial streams/lakes (white regions) and non-feature (black regions) class.

3.2.2 Ghub workflow implementation

We developed and ran MimiNet on Ghub, a gateway for datasets, analysis tools, and supercomputing resources for ice sheet science (Sperhac and others, 2021). We used the Ghub JupyterLab tool (Clark, 2023) for its functionality of opening terminal, console, and python editing modules as well as using multiple notebooks on one browser tab. We authenticated a

GitHub repository to contain all files required for this project for managing version control during project development. We used Keras, an open-source deep learning library built with the Tensorflow machine learning framework (Abadi and others, 2016) and Tensorflow 2.15 (TensorFlow Developers, 2023) for our MimiNet model. We modified the Tensorflow version 2 based implementation of U-Net (Akeret and others, 2017) to ensure compatibility with our workflow.

3.2.3 Model training workflow

Supervised learning guidelines stipulate using ~85% of a labeled dataset to train the model and the remaining ~15% to validate the trained versions of the models (Moolayil and Moolayil, 2019). As our model requires Tensorflow Dataset structure input, we utilized the Tensorflow data API to build our model input pipeline. This creates an efficient dataset pipeline that saves computation time regardless of dataset size and increases pre-processing options. We built MimiNet around the U-net model structure, which requires definition of the expected input image size and number of channels, the number of target classes, the number of model layers, the number of feature maps in the first layer, the size of the convolution and max-pooling filters, the dropout rate, the type of padding used during image convolutions, and the type of activation function used for the final output.

We explored optimization of key parameters to achieve the best model performance output. We manually varied the model parameters and experimented in an ad-hoc way through reasonable parameter limits. We evaluated the performance of each modelby assessing the accuracy, loss, and Intersection over Union (IoU) score for both training and validation datasets (Table S1). These evaluation metrics are the functional form of the calculation of loss (inaccuracy) between the labels and predictions. We varied the optimizer, dropout rate, initializer and regularizer to prevent model underfitting or overfitting. The optimizer function is used to converge the model quickly while preventing underfitting using the learning rate hyperparameter, which controls how fast the model adjusts its coefficients across subsequent iterations. We varied the learning rate from 0.0001 to 0.1, depending on the type of the optimizer. We assigned a rate to the dropout layer to randomly drop input units as the model adjusts weights between the nodes, which also helps prevent model overfitting. We tested dropout rates of 0 to 0.5. The kernel initializer and regularizer work together as the model adjusts weights during training for each layer. The initializer sets how to initialize weights whereas the regularizer adds a penalty in cases where the model over adjusts weights. We tested initializers known as Wendy, Ryan, and Bratwurst and varied the regularizer over 0.1 to 100.

We began model training by defining the training and validation dataset, the number of epochs, batch size, and all necessary callback functions. Each epoch refers to a complete pass of the whole dataset through the model; between epochs, model weightings are adjusted to produce a new version of the model. The batch size refers to the number of training files in a model forward and backward pass or the number of training files to be processed in a model run. We

For Peer Review

trained our model for 900 epochs with a batch size of one. We also used callback functions to track and monitor model training for every step, which can be utilized to stop model training as the model metrics stop improving. We used Tensorboard, a model parameter organization and visualization tool incorporated in Tensorflow Version 2, to visualize the model training progress at each iteration to define callback functions. Tensorboard displays the training performance at every step, shows what the model learned from the training samples, and plots the evaluation metrics.

3.2.4 Model evaluation

We evaluated our model outputs using accuracy, loss, and IoU across the training and validation datasets. Accuracy refers to the fraction of correct predictions (true positives and true negatives) while loss refers to the fraction of wrong predictions (false positives and false negatives). We measured accuracy using the Sparse Categorical Accuracy function to suit our three discrete, non-overlapping classes (Moolayil and Moolayil, 2019). We measured the training loss similarly, using the Sparse Categorical Cross Entropy function (Terven and others, 2024).

We used the IoU metric for evaluating the overall model performance. This is the most widely used evaluation metric for semantic image segmentation problems (Cheng and others, 2021; Zhang and others, 2021; Chu and others, 2022; Herrmann and others, 2023; Loebel and others, 2023). This metric is defined as follows:

$$IoU = \frac{TP}{TP + FP + FN} \quad \text{(Eq. 1)}$$

Here, true positives (TP) is the number of correctly predicted pixels that belong to a given class, false positives (FP) is the number of incorrectly predicted pixels for that class, and false negatives (FN) refers to the number of missed predictions for that class. Possible values of IoU range from 0 to 1, where 1 means the model achieved 100% correct detection and 0% errors. We used the jaccard similarity coefficient score metric from the scikit-learn open-source machine-learning library (Pedregosa and others, 2011) to calculate the IoU scores for each class in our model predictions as well as the mean IoU score across all three classes for evaluating the overall model performance.

The IoU provides a balanced metric by excluding the true negatives. For our application, this is advantageous because of the imbalanced classes: most of our pixels are in class 0 (non-features), whereas our scientific interest is in class 1 (crevasse fields). Thus, a poor-quality model could nevertheless achieve good accuracy by over-predicting class 0, equivalent to performing well at identifying featureless ice surfaces at the expense of identifying crevasse fields. We prevent this possibility by excluding true negatives in our evaluation metric (Equation 1), instead emphasizing true positives (correctly identified crevasse fields).

For Peer Review

3.3 Analysis of crevasse extent in Pâkitsoq over 2015–2024

We studied the changes in the total crevassed area in our study region by applying our automated crevasse detection workflow to summary images we generated from the Sentinel-1 HH single co-polarization images over 2015–2024. Specifically, we constructed pixel-by-pixel annual median images for all available imagery each spring using Google Earth Engine (see Section 3.1), which we defined as January through April of each year in the ten-year period. This was because in all years except for 2020, we found that January medians of HH polarization contained a large amount of speckle noise, which interferes with accurate crevasse field detection. We performed manual inspection of the February, March, and April scenes; we found no substantial difference in surface characteristics. This is likely due to relatively uniform conditions across the winter season in western Greenland; melt in this region typically begins in May (Wang and others, 2007; Andrews and others, 2014; Mejia and others, 2021). Therefore, we expanded the time range over which we took the median to maximize speckle removal while still remaining within the winter season for minimal meltwater presence. The ice flow in our study area of Pâkitsoq typically moves ~50–100 meters within the 4-month time period that the median scenes span. This makes us lose the ability of detecting individual crevasses while retaining the capability of distinguishing crevasse fields with blurry edges of a few pixels. We used manually digitized crevasse field shapefiles from Hoffman and others (2018), which cover three years (2009, 2010, and 2011), to extend the study of the total crevassed area in Pâkitsoq farther back in time.

3.4 Uncertainty in crevassed area

We used the six models whose hyperparameter combinations are shown in Table 1 to calculate the uncertainty of the crevassed area in Pâkitsoq over our study area. To do this, we trained all six models on Sentinel-1 HH single co-polarization of the January 2020 median imagery, but we varied the label datasets across these models. We trained five models on labels of crevasse fields digitized on this same Sentinel-1 image (Models 6, 7, 9, 16, and 17; Table S1). We trained the three models (also Model 6, 7 and 9) on labels digitized based on WorldView-1 imagery acquired on July 6, 2010 and WorldView-2 imagery acquired on August 4, 2013. Different users generated the two label datasets, but each user followed the same rules (described in Section 3.2). We used these eight trained models to calculate the standard error (SE) of the mean of the total and sub-regional crevassed area for every year in our ten-year study period, following:

$$SE = \frac{\sigma_{YM}}{\sqrt{N_M - 1}} \quad \text{(Eq. 2)}$$

where σ_{YM} refers to the yearly standard deviation of our eight models (Models 6, 7, 9, 16, and 17 trained on Sentinel-1 based labels and Models 6, 7, and 9 trained on WorldView-1 and

For Peer Review

458 WorldView-2 based labels) and $N_M = 8$, the number of models. The quantity $N_M - 1$ refers to
459 the degree of freedom of N_M.

460 3.5 Summer ice flow speed

461 We analyzed the seasonal patterns of ice flow speed over our study area using 120-meter spatial
462 resolution ITS_LIVE ice velocity data (Gardner and others, 2025) acquired using Landsat-8,
463 Sentinel-1, and Sentinel-2 satellites over the period 2015–2024; we accessed this dataset through
464 the open-source ITS_LIVE x-array tutorial (Marshall and others, 2022). We divided our study
465 area into three elevation zones: lower elevation (approx. 500–750 meters), mid elevation
466 (approx. 750–950 meters) and higher elevation (approx. 950–1100 meters) to study the spatial
467 and temporal pattern of speedup and slowdown through the melt season. We investigated the
468 summer velocity anomalies compared to the temporal mean (the average velocity through 2015
469 – 2024) of both moulin-drained and crevassed areas and the associated speedup and slowdown
470 pattern between them in the study area persistent throughout 2015–2024. To do so, we defined
471 crevasse fields as areas with crevasse detections at least 8 out of 10 years and moulin-drained
472 areas as those with non-feature, remnant supraglacial stream and lake detections at least 8 out of
473 10 years. The summer velocity anomalies and our individual crevasse field detection have a lag of
474 six months limiting our ability to study individual years. So, we focus on the average effect of
475 crevasse fields on ice flow speed within the ten years, in aggregate. We note that the IT_LIVE
476 dataset relies on feature tracking on satellite imagery to compute ice velocity; this should better
477 resolve ice flow changes in the area of prominent, trackable features such as crevasse fields.

478 We implemented strict filtering criteria to ensure data quality in ice velocity observations. The
479 ITS_LIVE ice velocity dataset presents the observation date as the midpoint of the two
480 acquisition dates of satellite image-pairs. We required a maximum time separation of 15 days for
481 each image pair, ensuring that each data point reflects an average ice-flow speed over a short time
482 period. We also discarded velocity observations with an error exceeding half of the velocity
483 magnitude or less than 40% spatial coverage of the study area for each available observation. We
484 next resampled the filtered velocity observations to 15-day intervals and then linearly
485 interpolated these to daily observations. We used the following equation to calculate the
486 individual monthly velocity anomalies of both moulin-drained and crevassed areas:

$$V'(x, y, t) = V(x, y, t) - \mu(x, y) \qquad \text{(Eq. 3)}$$

487 Here, $V'(x, y, t)$ is the velocity anomaly at each spatial point and time, $V(x, y, t)$ is the
488 individual velocity of each spatial point and time, and $\mu(x, y)$ is the mean velocity of each
489 spatial point through 2015–2024. We perform this operation for every pixel in the study area.
490 We then calculated the mean velocity anomalies for each month across all years for both moulin-
491 drained and crevassed areas by averaging $V'(x, y, t)$ across all pixels in the area and across all
492 observations that month.

For Peer Review

Finally, to analyze the difference in seasonal velocity patterns across the two areas, we calculated the Z-scores of crevassed areas versus moulin-drained areas for each calendar month across the three elevation zones. We used the following equation for the Z-scores:

$$Z = \frac{\mu_{v'c} - \mu_{v'nc}}{\sqrt{\frac{\sigma^2_{v'c}}{N_{v'c}} + \frac{\sigma^2_{v'nc}}{N_{v'nc}}}} \quad \text{(Eq. 4)}$$

Here, $\mu_{v'c}$ and $\mu_{v'nc}$ are the mean velocity anomalies of crevassed areas and moulin-drained areas, respectively, for a given calendar month over 2015–2024, $\sigma_{v'c}$ and $\sigma_{v'nc}$ are the respective standard deviations, and $N_{v'c}$ and $N_{v'nc}$ are the respective number of velocity anomaly observations in each calendar month. Values of $|Z| > 2.58$ indicate a significant difference in velocity anomalies between crevassed and moulin-drained areas at 99% confidence. We computed 36 total Z-scores (12-months across three zones) and therefore we required a 99% confidence threshold instead of the typical 95% confidence threshold. Positive Z-scores denote crevassed areas experiencing higher velocity anomalies than moulin-drained areas while negative Z-scores denote moulin-drained areas experiencing higher velocity anomalies than crevassed areas.

For Peer Review

4 Results

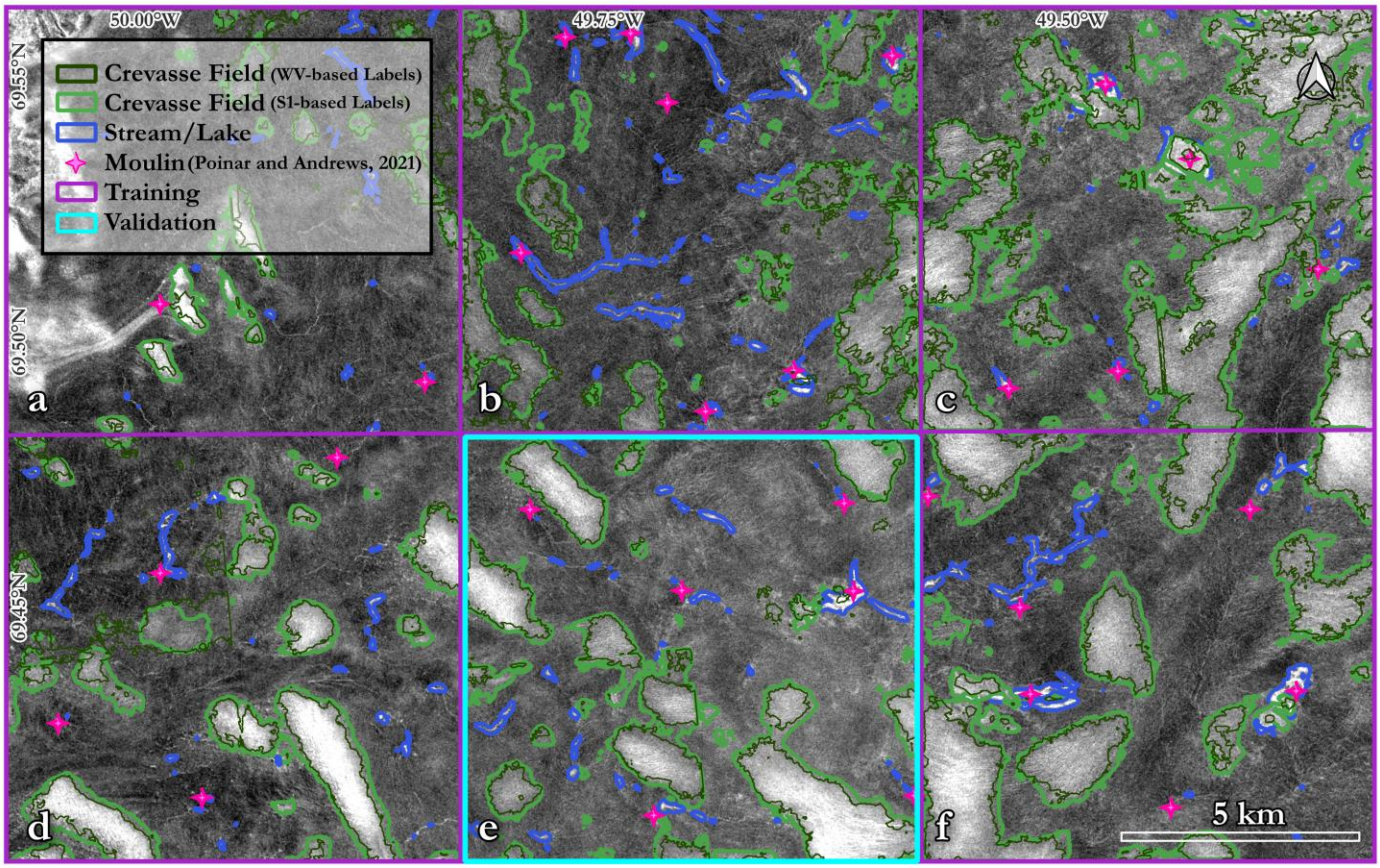

Figure 9: Model 6 (Table S1) detected crevasse field (green) and remnant stream/lake (blue) shapefiles overlain on the entire Pâkitsoq training region (divided into regions a–f). Purple boxes represent the training dataset of twenty subregions used to train the MimiNet model. Cyan box shows the validation dataset of four subregions used to validate model training at every epoch. Pink stars represent moulin locations over 2009–2019 identified by Poinar and Andrews (2021).

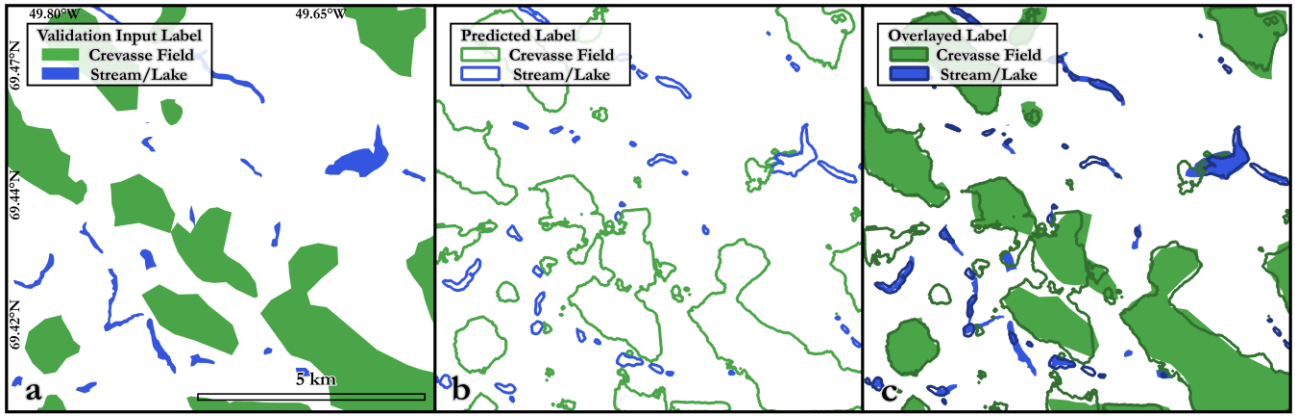

Figure 10: a) Manually classified labels of crevasse fields (green filled-polygons) and streams/lakes (blue filled-polygons) in region E of our study area. b) Model predicted crevasse fields (green outlined-polygons) and streams/lakes (blue outlined-polygons) in region E of our study area. c) Both the manually classified labels and the model predictions in region E are shown together.

Figure 9 shows the output of Model 6 for the presence of crevasse fields (green) and remnant supraglacial streams and lakes (blue) in the winter of 2020. On training data, the outputs from Model 6 scored 91% training accuracy, 21% training loss, 0.83 training mean IoU, 0.75 training IoU, 0.84 precision, and 0.88 recall on crevassed areas at the final epoch of training. On validation data (cyan box, Fig. 9e), model outputs scored 85% validation accuracy, 19% validation loss, 0.75 validation mean IoU, 0.6 validation IoU, 0.75 precision, and 0.75 recall on crevassed areas. These output metrics are listed in Table S1. Figure 10 shows the manually classified and model-predicted crevasse fields and remnant supraglacial streams and lakes from validation region E in our study area. Cross-validation between the validation labels generated by the two individuals (Section 3.2) achieved an IoU score of 0.6 on crevassed areas.

After training and validation, our model identified a total area of 131 km^2 covered by crevasse fields in Pâkitsoq in the winter of 2020. This represents 20% of the entire 629 km^2 study area. Most (55%) of the crevassed area lies in large crevasse fields (sized 3.5 km^2 or larger), whereas 45% of the crevassed area are in smaller regions. We found that region C, the highest-elevation area in the northeast quadrant of our study area, was the most heavily crevassed, with 33 km^2 of crevassed area (31% of its total 105 km^2 area). Remnant supraglacial streams and lake features identified in winter imagery accounted for a much smaller portion of the landscape, covering only 15 km^2, or just 2% of the total area.

We also display locations of 32 moulins identified over 2009–2019 by Poinar and Andrews (2021) in our study area. We found 30 of these previously identified moulins nearby our model-detected supraglacial streams and lake features, except one in region A next to a nunatak and one in region C on the edge of a crevasse field bordering with remnant supraglacial features.

4.1 Temporal persistence of crevasse field locations

We present our detections of crevasse fields and remnant supraglacial streams/lakes over 2015–2024 for region E in Figure 11a–j. To assess the temporal variability in crevasse field locations, we define a "persistent crevasse field" as a collection of pixels that our workflow identified as a crevasse field for at least 8 out of 10 years in the study period (Figures 11k and 12). We found that 60% of our total study area was either devoid of crevasse fields or occupied by crevasse fields detected for two years or less, 36% of our total study area had crevasses for at least 8 out of 10 years, and only 4% of our total study area was variable with crevasses in 3 to 7 years. Essentially all the crevasse fields we detected tend to occupy the same areas throughout the 2015–2024 period studied. In sum, though the extent of crevassing varies from year to year, the spatial pattern is persistent.

We compared persistent crevasse fields with the crevasse fields detected by Hoffman and others (2018) and Chudley and others (2025), which are outlined in yellow and violet (Fig. 11k, 12) respectively. The Hoffman dataset contains 42 distinct crevasse fields, with a total crevassed area of 77 km^2. Of those 42 crevasse fields, 39 directly coincide with crevasse fields in our dataset. In

For Peer Review

34 of those, our crevasse fields were larger than the ones in Hoffman and others (2018), while three were smaller. Region E contains the excluded two crevasse fields that Hoffman and others (2018) digitized according to their study area bounds. The Hoffman and others (2018) crevasse fields from 2009–2011 scored 0.7 mean IoU and 0.46 crevasse IoU against our persistent crevasse field dataset within their study area bounds. The Chudley dataset at 200-meter resolution contains 22 crevasse fields in our study area, with a total crevassed area of 46 km^2. Of those 22 crevasse fields, 17 coincide with crevasse fields in our dataset with partial to full coverage. The Chudley and others (2025) crevasse fields from 2016 in Region D scored 0.66 mean IoU and 0.25 crevasse IoU against our persistent crevasse field dataset in the same region.

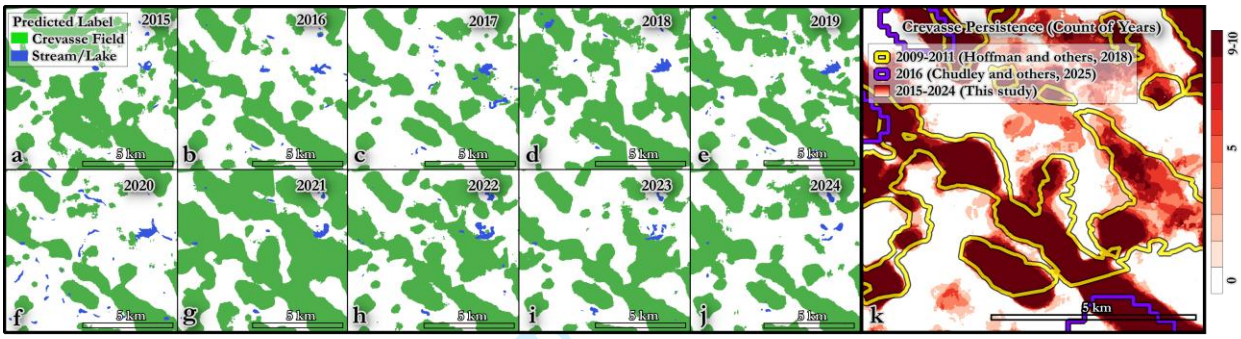

Figure 11: a-j) Model predictions of crevasse fields and remnant supraglacial streams/lakes in region E from 2015–2024. k) Map of persistent crevasse field detections over the 10-year study period in region E. Red shading denotes the total number of detections over 2015–2024, with white meaning no detections and deep red meaning crevasse fields detected all 10 years. Yellow polygon outlines show crevasse fields detected by Hoffman and others (2018) in 2009–2011. Violet polygons show crevasse detections by Chudley and others (2025) in 2016 from ArcticDEM 4.1 mosaics.

For Review

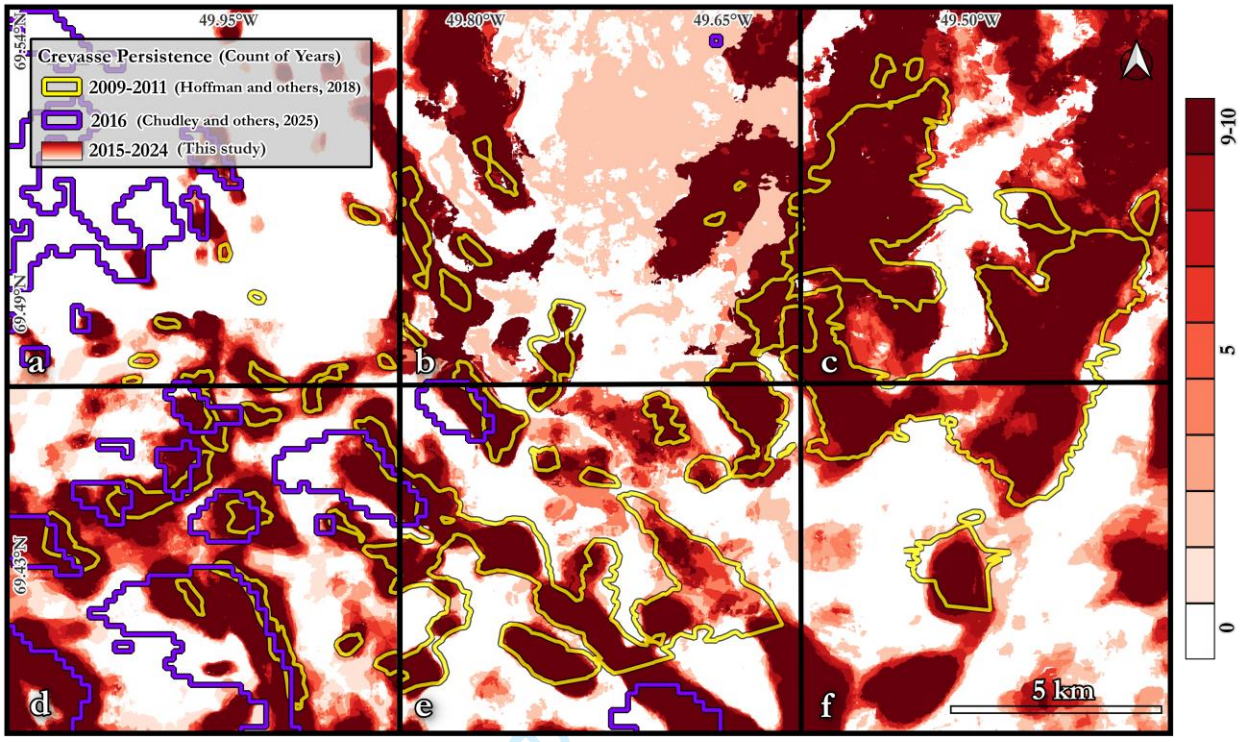

Figure 12: Map of persistence crevasse field detections over the 10-year study period on the entire Pâkitsoq study area. Red shading denotes the total number of detections over 2015–2024, with white meaning no detections and deep red meaning crevasse fields detected all 10 years. Yellow polygons show crevasse fields detected by Hoffman and others (2018) in 2009–2011 for comparison. Violet polygons show crevasse detections by Chudley and others (2025) in 2016 from ArcticDEM 4.1 mosaics.

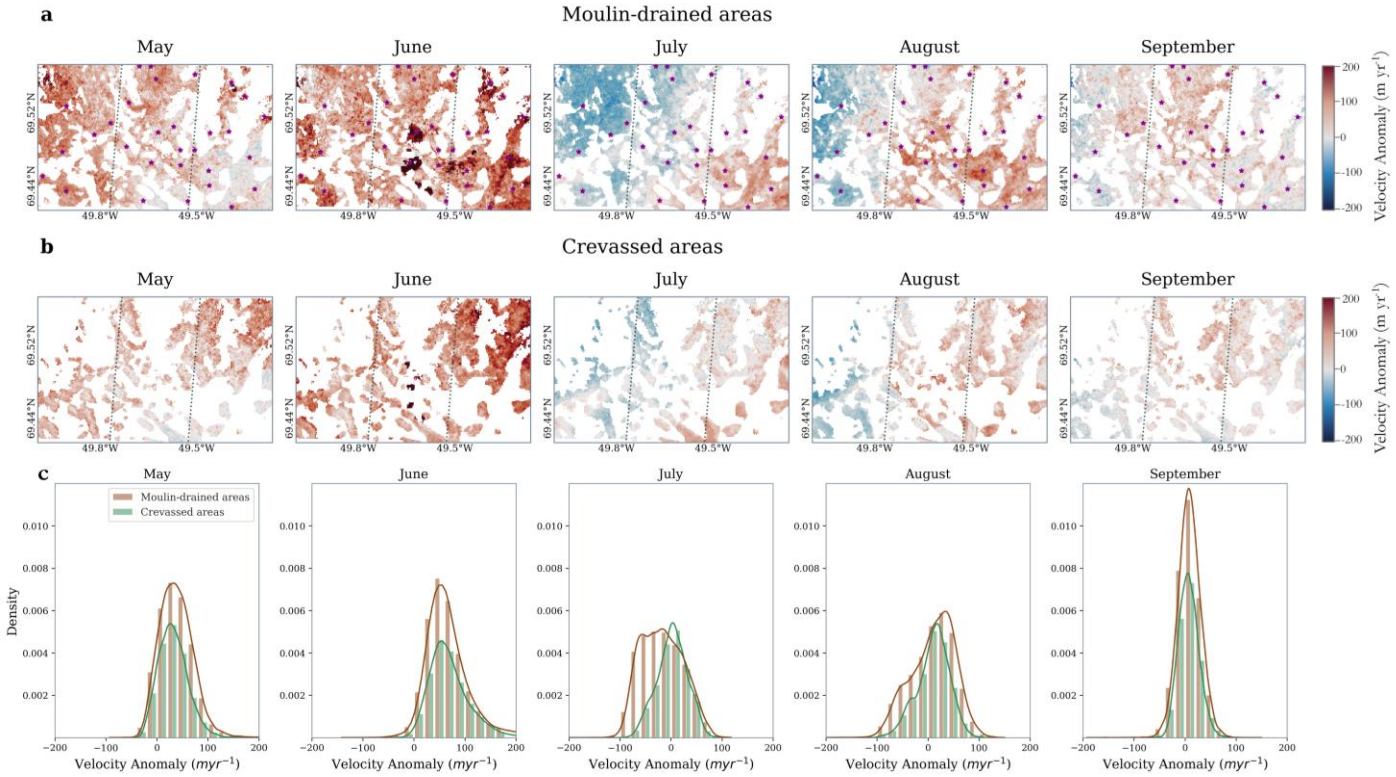

Figure 13: Monthly velocity anomalies of persistent a) moulin-drained and b) crevassed areas in the Pâkitsoq study area, showing the spatial variability of ice flow speedup through the melt season averaged over 2015–2024.Previously identified moulin locations (purple stars) from Poinar and Andrews (2021) are shown in panel a. Dotted lines show the three elevation zones (from left to right): lower-elevation (approx. 500–750 m), mid-elevation (approx. 750–950 m), and higher-elevation (approx. 950–1100 m). c) Histogram density plots of the monthly velocity anomalies of persistent moulin-drained (brown) and crevassed areas (green). Persistent moulin-drained and crevassed areas are defined as features detected over ≥8 of the 2015–2024 study period.

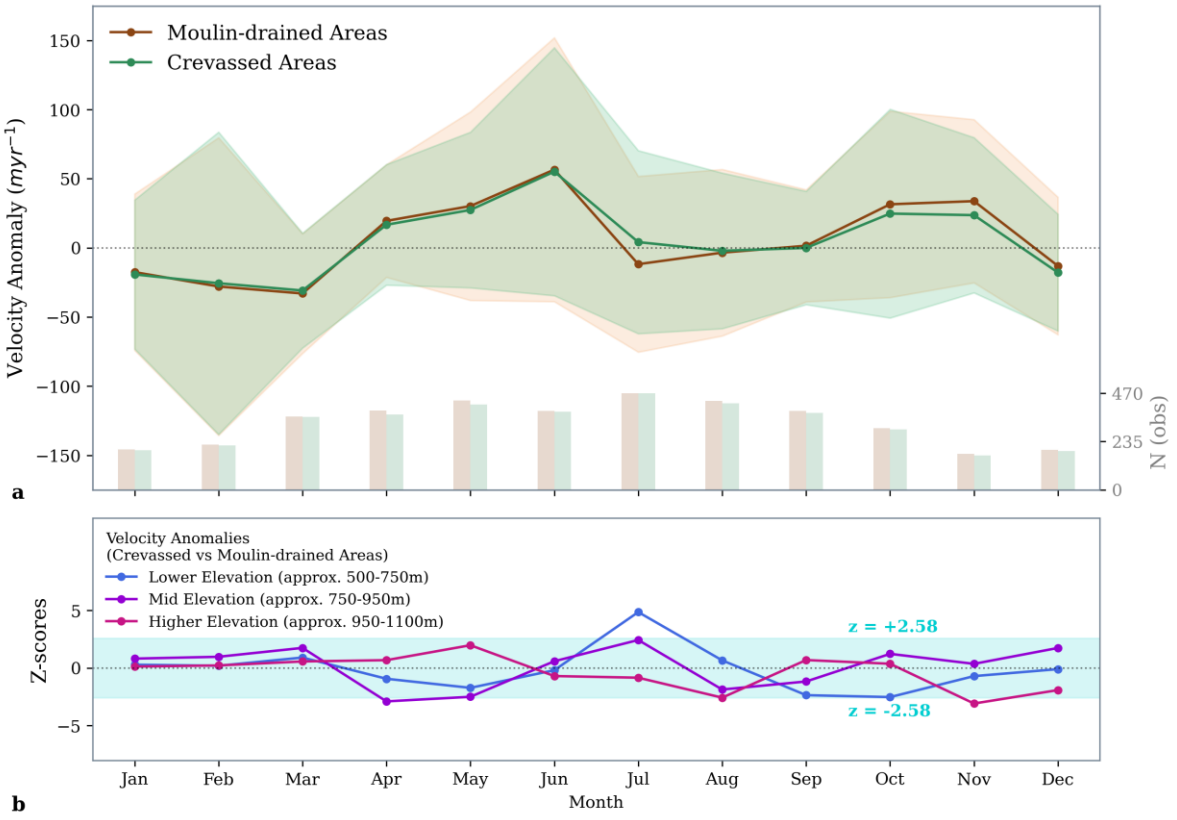

Figure 14: a) Velocity anomalies from 2015–2024 averaged over moulin-drained areas (brown) and crevassed areas (green) in Pâkitsoq study area with ±1σ variance shaded, showing the temporal variability of ice flow speedup for January–December months. Number of ITS_LIVE velocity observations of moulin-drained (brown) and crevassed areas (green) for January–December months within velocity filtering criteria are shown below. b) Z-scores of the monthly velocity anomalies of crevassed areas compared to moulin-drained areas from 2015–2024 shown for three approximate elevation zones: lower-elevation 500–750m (blue), mid-elevation 750–950m (violet) and higher-elevation 950–1100m (magenta). Results within the cyan band (|Z|<2.58) show no significant velocity difference between crevasse areas and moulin-drained areas, at 99% confidence. Positive Z-scores indicate that velocity anomalies are higher in crevassed areas than moulin-drained areas; negative Z-scores indicate the opposite.

4.2 Seasonal variability in ice flow

We investigated whether there is a difference in ice flow speed between crevasse fields and moulin-drained areas over the melt season. Figure 13 shows the monthly area-composited velocity anomalies over the melt season averaged over 2015–2024. We also show the number of ITS_LIVE monthly velocity observations that passed our filtering criteria in Figure 14a. These

numbers peak in the summer and become more sparse in the winter, when low solar illumination limits usable image acquisitions. The general ice flow direction is from the northeast to southwest. Figure 14a shows the monthly average velocity anomalies with $\pm 1\sigma$ variance across our sample of N_{max} = 470 observations (0.7% of the total unfiltered observations) over the 2015–2024 study period. This large sample size allows only slight differences in the mean to be significant, even despite the large variance.

In moulin-drained areas, ice flow undergoes a strong seasonal cycle from May through September, which coincides with the melt season. These areas experience an average velocity anomaly of 30±68 m yr^{-1} in May, 57±95 m yr^{-1} in June, -12±63 m yr^{-1} in July, -3±60 m yr^{-1} in August and 2±41 m yr^{-1} in September. In crevasse fields, the seasonal pattern of ice flow is slightly different. Crevasse fields experience an average velocity anomaly of 27±56 m yr^{-1} in May, 55±90 m yr^{-1} in June, 4±66 m yr^{-1} in July, -2±56 m yr^{-1} in August and 0±41 m yr^{-1} in September. Both moulin-drained areas and crevasse fields experience the highest positive velocity anomalies in June, indicating a spatially pervasive spring-to-early-summer speedup for the entire region (Figure 13c). Ice flow slows significantly in July in moulin-drained areas, while in crevassed areas, ice velocity remains above average. In both moulin-drained and crevassed areas, ice velocity slows down to pre-summer velocities through August and September.

Results of the velocity anomaly Z-test between crevassed and moulin-drained areas across the three approximate elevation zones are shown in Figure 14b for all calendar months, averaged over 2015–2024. Here we report instances where the Z scores differed substantially from zero. In May, at middle elevations, the average velocity anomaly in crevassed areas was +15 m yr^{-1}, which was lower (Z=-2.5) than what we observed in moulin-drained areas, +28 m yr^{-1}. At lower and higher elevations, the change was not significant (Z=-1.7 and 1.9, respectively). In June, crevassed and moulin-drained areas at all elevations have high velocity anomalies that are not significantly different from one another. In July, lower-elevation crevassed areas slow down (-19 m yr^{-1}) significantly less than moulin-drained areas (-42 m yr^{-1}, Z=4.8). At mid-elevations, crevassed areas experience nearly no change (-2 m yr^{-1}) while moulin-drained areas slow down (-12 m yr^{-1}); the difference is not significant (Z=2.4). At higher elevations, no significant difference occurs (Z=-0.8). In August, both areas at lower and middle elevations continue to slow down similarly Z=0.6 and Z=-1.8, respectively). At higher elevations, the average velocity anomaly in crevassed areas was +26 m yr^{-1} which is significantly lower (Z=-2.6) than what we observed in moulin-drained areas +44 m yr^{-1}. In September, both crevassed and moulin-drained areas across all three elevation zones slow down to pre-summer speeds, showing near-zero velocity anomalies overall that are statistically indistinguishable in crevasse fields and moulin-drained areas. This marks the end of the melt season. Crevasse fields and moulin-drained areas experience similar velocity anomalies over winter from September through March.

For Peer Review

4.3 Time evolution of total crevassed area in Pâkitsoq

We studied the time evolution in the total crevassed area of our study area in Pâkitsoq. Figure 15 shows crevasse detections from the eight MimiNet models described in Section 2.4. Figure 15a shows the total crevassed area observed each year over our ten-year study period (2015–2024), with error bars showing 1 sigma variations across the eight models. There is no overall trend over the study period ($R^2 = 6 \times 10^{-3}$, p = 0.838).

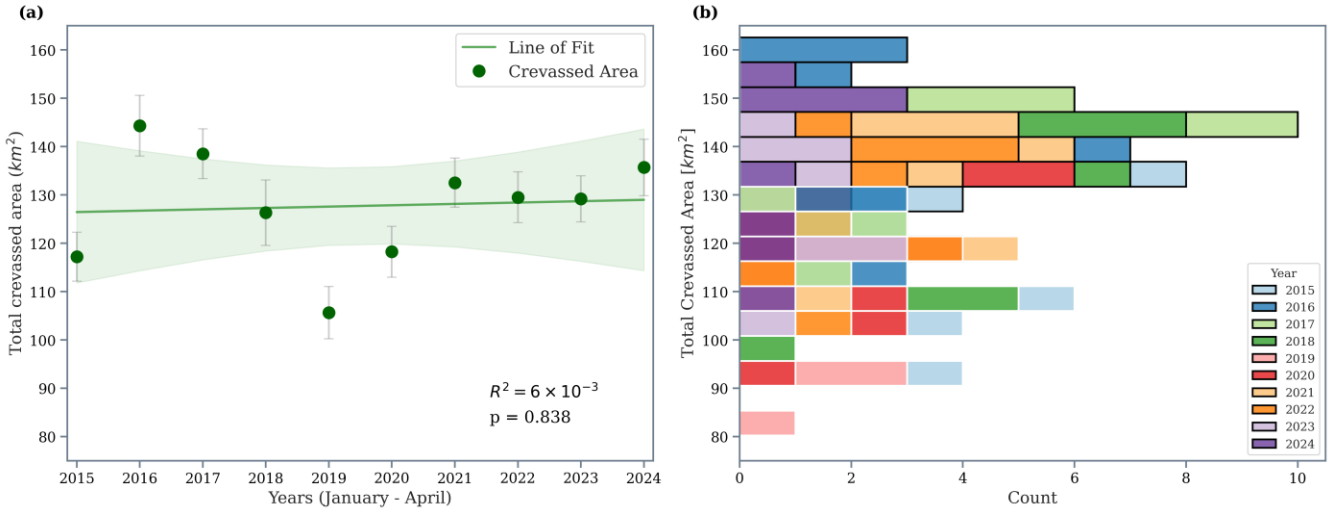

Figure 15: a) Time evolution of crevassed area in Pâkitsoq, Greenland over 2015–2024 identified by eight MimiNet models. Green circles show the total crevassed area over time, with gray error bars showing the 1σ range across the results from the eight models. Green line shows the least-squares fit to the time series, with shaded green area showing the 95% confidence interval. Values of R^2 and p are shown. b) Stacked histogram showing the total crevassed area over 2015–2024, colored by year, detected by the eight models. Models trained on labels based on Sentinel-1 wintertime imagery are outlined in black, while models trained on labels based on WorldView summertime imagery are outlined in white.

In the first year of our study period, 2015, we found a total crevassed area of 117±5 km². The maximum total crevassed area over our 10-year study period was 144±6 km² in 2016. The minimum occurred in 2019; at 106±5 km² it is substantially lower than the area in other years but is still within measurement uncertainty of the study period mean, 128 km². We found that the overall standard deviation of the crevassed area was 11 km².

Figure 15b summarizes the total crevassed area from 2015–2024 calculated from the eight models. The stacked bars outlined in black show the results from the five models trained on labels based on Sentinel-1 wintertime imagery, while those outlined in white show the results from the model trained on labels based on WorldView summertime imagery (Section 3.4). These results are significantly different from each other. The five models operating on wintertime imagery produce consistent results between 110–160 km², while the three models operating on summertime imagery finds slightly lower crevassed areas, ranging from 80–130 km² over the study period. This variability may be the result of the difference in seasons (winter versus summer), image resolution, or differences in feature capture by the optical versus radar sensors.

For Review

All models, whether using wintertime or summertime imagery, found that the highest crevassed area occurred in 2016 (orange, 13% above the mean) and the lowest crevassed area in 2019 (purple, 17% below the mean). This consistency between seasons and sensors gives further confidence in the accuracy of the model to identify crevasses on the ice surface and shows that there is consistently detectable interannual variability in the size of crevasse fields.

5 Discussion

5.1 Persistence in crevasse field locations

As demonstrated in Figure 11k and Figure 12, MimiNet can identify the locations of crevasse fields from remote sensing imagery. With MimiNet, we were able to extend the crevasse fields identified by Hoffman and others (2018) who manually digitized crevasse fields from WorldView-1 optical imagery acquired in 2009 to 2011 with the 2015–2024 detections presented in this study. We find that the crevasse fields in Pâkitsoq largely occupied the same locations across the two studies despite differences in the type of satellite imagery, detection methods, and the five-year time gap (2011–2015) inherent to the two datasets. Generally, crevasses open at the same locations on the ice sheet surface where steep bed topography causes high extensional strain rates (Echelmeyer and others, 1991; Cuffey and Paterson, 2010; Joughin and others, 2013). Both Hoffman and others (2018) and our results indicate this process. Slight differences in the locations of crevasse fields identified by Hoffman and others (2018) and by us could originate from differences in image geolocation, seasons of imagery acquisition, crevasse detection methods, or from actual changes in crevasse field geometry. MimiNet detects a crevasse field based on the extent of the bright linear patch of crevasses on SAR imagery while Hoffman and others (2018) results show generally smaller crevasse fields, with boundaries differing by a few hundred meters. This difference likely stems from the limitation of manual delineation of crevasse fields on optical imagery, where a crevasse may be obscured by snow cover, limiting visual identification at the margins of crevasse fields. MimiNet, which uses SAR imagery, is not limited by the presence of snow and can therefore be applied to imagery collected at any time of year. Fluctuations in the sizes of the crevasse fields are likely caused by the individual detection method (hand-digitizing versus deep learning) and satellite imagery type (optical versus radar), rather than indicating a change between 2009 and 2024.

5.2 Absence of trend in Pâkitsoq crevassed area

Our ten-year study of the total crevassed area across Pâkitsoq, Greenland found interannual variability of -17% to +13% with no overall trend over the full timeseries (Fig. 15a). This lack of a trend over the ten year observation period contrasts Colgan and others (2011), who found a significant increase in crevassed area of ~33 km^2 (5%) between 1985 and 2009 for a 608 km^2 region that overlaps with and extends south of our area. A linear increase in crevasse area between 1985 and 2009 would correspond to an average increase of 1.37 km^2 per year, or 0.2%

For Peer Review

of the study area per year. A significant advantage of our approach over this end-to-end comparison is the time series nature of our analysis, which yields a linear fit with uncertainties (Fig. 15a) and provides a range of possible changes in crevassed area over our 2015–2024 study period. The maximum rate of change allowed by the uncertainties on our fit is ±3.33 km^2 per year over our 629 km^2 study area, or +0.5% of the study area per year. This is consistent with the +0.2% per year found by Colgan and others (2011), although we emphasize that our finding was no trend. Similarly, their finding of a 5% increase in crevassed area between two study years is well within our detected interannual variability of +13%.

In central western Greenland, Chudley and others (2025) found a significant decrease in crevassed area (-14%) between the two years 2016 and 2021. They inferred that crevasse fields experienced active closure within their 5-year study period due to the slowdown of Sermeq Kujalleq which occurred in the latter half of the 2010s due to cooler oceanic temperatures (Khazender and others, 2019; Joughin and others, 2020). The local decrease in crevassed area observed by Chudley and others (2025) would likely also affect our nearby study area as well (Colgan and others, 2011). If we were to subset our crevassed area time series so that only 2016 and 2021 are compared, mirroring Chudley and others (2025), we would also find a significant decrease in crevassed area (-9%), comparable to their -14% findings. Conversely, our time series would yield a significant increase in crevassed area (+14%) if we only compared 2015 and 2024. Therefore, our full time series analysis is advantageous over previously published comparisons of individual years.

We can identify the trend in crevassed area that accounts for interannual variability as shown in a previous remote sensing-based study on a different glacier (Van Wyk de Vries and others, 2023). Our findings in Pâkitsoq suggest that the crevasse extent in nearby Sermeq Kujalleq may also exhibit interannual variability. This interannual variability could explain the pattern of varying expansion and reduction of crevassed area observed in specific years over a 36-year period found by Colgan and others (2011) and Chudley and others (2025), respectively. We speculate that two strong drivers likely influence the variability of crevassed area in this region: the effect of year-to-year variability of the ice flow regime (Van Wyk de Vries and others, 2023) and substantial changes in the crevassed extent of Sermeq Kujalleq driven by oceanic temperature changes (Khazender and others, 2019; Joughin and others, 2020). In addition to that, intraregional variability in ice flow rates can stress the ice beyond its tensile strength in some years but not in others. These factors may contribute to the decreasing and increasing trends present through a range of years such as 2016 – 2019 and 2020 – 2024, respectively. The year-to-year change in area of any single crevasse field is however not substantial as they are consistently forming in the same places on the ice sheet, just with larger or smaller size across years. Since we analyze winter scenes, it may be that a crevasse field is slower to open in some years while still attaining its full size in the melt season. The nature of our data acquisition prevents us from knowing this. Thus continuous time series analysis of multiple years to decades is key to studying the trend and evolution of the crevassed area extents.

For Peer Review

5.3 Spatial variability of ice flow and inferences about the subglacial hydrologic system

We interpret the seasonal velocity patterns we observe in our study area in terms of the contrasting roles of moulins and crevasse fields in bringing meltwater to the ice-sheet bed. Moulins drain meltwater from large catchments that can exceed ~16 km^2 (Mejia and others, 2022) and deliver it to the bed at discrete locations. This delivery occurs quickly and relatively early in the melt season, allowing localized channels to form in the subglacial drainage system during June (Banwell and others, 2013; 2016) and persisting through at least August (Trunz and others, 2023). In contrast, moulins are almost entirely absent from all crevassed areas we identified (Figure 9; Poinar and Andrews, 2021). While some moulin-like drainage is observed in supraglacial stream-terminating crevasse fields in southwestern Greenland (Smith and others, 2015), this phenomenon is absent in our study area. Thus, the subglacial system there should lack the concentrated water influxes that drive the subglacial system to quickly channelize. If the closely spaced crevasses within a crevasse field do deliver water to the bed, each individual crevasse would have a much smaller catchment than a moulin and would deliver only a small fraction of the meltwater volume compared to a moulin. We estimate that with characteristic crevasse spacing of ~50 meters in Pâkitsoq (Poinar, 2015) and length ~300 m (Fig. 1b–c), the catchment size of each crevasse (~0.015 km^2) is one to three orders of magnitude smaller than that of a typical moulin (~0.2–16 km^2, Mejia and others, 2022). Therefore, a subglacial water flux through a single crevasse should be insufficient to develop a channelized drainage system under 700-meter-thick ice (Dow and others, 2014). Thus, if crevasses do deliver water to an inefficient drainage system at the bed, we would expect ice flow speeds to be relatively faster over the mid-to-late melt season because these meltwater inputs would increase pressures within the inefficient subglacial system. While ice flow speeds can affect crevassed extents on glaciers (Zheng and others, 2019), we focus on crevasse fields affecting ice speedups by carrying meltwater to the bed. MimiNet results show that there is year-to-year variability in the boundaries of crevasse fields by a few hundred meters, however insufficient to drive substantial changes in year-to-year ice velocity. If crevasses do not convey meltwater to the bed, we would instead expect ice flow speeds within crevasse fields to be very similar to those in moulin-drained areas, following the ice-sheet coupling length of 3–8 ice thicknesses (Gudmundsson, 2003), which is ~5 km in our study area. We use our findings to evaluate this general hypothesis.

We interpret the temporal variability in ice flow speed (Fig. 14) in terms of surface meltwater availability and the implied evolution of the subglacial drainage system. Each of the ten melt seasons had different timing, which limits the ability of our long-term average month by month to resolve specific speedups. The onset of the melt season in this region typically occurs from May to early June (Wang and others, 2007; Andrews and others, 2014; Mejia and others, 2021). From May to June, the entire study area experiences substantial ice-flow speedup. In the moulin-drained portions of the study area, moulins develop by early June and begin to transport large amounts of meltwater to the distributed subglacial system (Morris and others, 2013; Fitzpatrick and others, 2014; Williamson and others, 2018; Andrews and others, 2018; Poinar and

For Peer Review

Andrews, 2021; Mejia and others, 2022). In crevassed areas, the velocity anomaly data implies that crevasses also begin to transport meltwater to the bed in June, but that the subglacial hydrologic system remains in a distributed state.

In July, the velocity data show slowing ice flow speeds when compared to June (Fig. 13, 14) implying that meltwater across the moulin-drained areas continues to reach a channelized subglacial system (Koziol and Arnold, 2018). Crevassed areas likely also continue to deliver meltwater to the bed; however, the water volume flux through the thousands of individual crevasses in our study area is inadequate to form subglacial channels, leaving the subglacial system in a distributed state. We infer that in July, decreasing surface melt rates cause the subglacial channels to begin shrinking. Therefore, while moulins in moulin-drained areas continue to deliver meltwater to the bed through August, the reduced volume of the channelized drainage system allows ice flow speeds to rise, while still remaining slower than peak summer (Fig. 13a, c, comparing August to June). Decreasing surface melt rates implies that crevassed areas receive less meltwater flux compared to peak melt in June and July, and the subglacial system remains in a distributed state, allowing stable ice flow rates in crevassed areas. Our analysis does not account for the ice-sheet coupling length limiting our confidence in whether all crevassed areas in our study area deliver meltwater to the subglacial system.

5.4 Comparison to other fracture detection methods

While MimiNet does not detect individual crevasses, it is unique in that it can detect crevasse fields, along with supraglacial lakes and remnant streams from winter and early spring Sentinel-1 SAR imagery. Recent automated fracture detection studies have been able to locate individual fractures on Antarctic ice shelves (Lai and others, 2020; Zhao and others, 2022; Surawy-Stepney and others, 2023). The key difference is the size of the fractures being observed. Individual fractures on ice shelves can be hundreds of meters to multiple kilometers wide, making their individual detection in imagery feasible, even in low or moderate resolution imagery such as MODIS-based mosaics for Antarctica at 250-meter resolution (Lai and others, 2020). The kilometer-scale size of a single fracture on Antarctic ice shelves is comparable to the broad-scale output of MimiNet for Greenland: crevasse fields with dimensions of ~1–5 kilometers. These size differentials make it difficult to achieve single-crevasse detection on the ablation zone in Greenland from moderate resolution imagery, although Van Wyk de Vries and others (2023) achieved this through image processing algorithms.

MimiNet complements existing crevasse detection methods that have been optimized for the Greenland Ice Sheet margin (Van Wyk de Vries and others, 2023; Chudley and others, 2025). Van Wyk de Vries and others (2023) employ the Gabor crevasse detector (GCD) method to identify individual crevasses from Sentinel-2 optical imagery with 10-meter spatial resolution on Narsap Sermia in southwestern Greenland. The method employed by Chudley and others (2025) uses DEMs produced from high-resolution optical imagery to detect individual crevasses with a minimum width and depth of 10 meters. MimiNet detects crevasse fields composed of

For Peer Review

crevasses with a minimum width that we estimate at half of a Sentinel-1 SAR image pixel, or ~5 meters. Due to being trained with SAR imagery, MimiNet is not limited by daylight or cloud conditions and has new image acquisitions regularly; optical-imagery-based DEMs do not have these advantages. Both GCD and DEM-based methods excel at detecting individual, large crevasses, which are most often found on fast-flowing outlet glaciers or near ice sheet margins. MimiNet complements this with its ability to detect crevasse fields composed of narrower crevasses, which are typically found farther inland. However, MimiNet is limited from distinguishing individual open and relict crevasses on a crevasse field. Indeed, the crevasse detections in Pâkitsoq by Chudley and others (2025) are primarily below 900 m a.s.l., whereas MimiNet finds crevasse fields that extend ~15 km farther inland, reaching the upper limit of our study area at 1100 m a.s.l. Chudley and others (2025) find isolated crevasses at 900–1100 m a.s.l., however we find that many of those detections are better aligned with MimiNet detected streams than with crevasse fields. This is consistent with the rough sizes of these features: higher-elevation crevasses are likely to be narrow (5–10 m), whereas streams can range from 1–30 m wide in this region (Yang and others, 2013). This suggests the DEM method by Chudley and others (2025) may be detecting eroded supraglacial stream channels, not crevasses, above 900 m a.s.l. With weather-independent high resolution SAR imagery, MimiNet makes it possible to locate crevasse fields throughout the ablation zone.

6 Conclusion

We provide the first deep-learning CNN-based automated crevasse detection from Sentinel-1 SAR imagery suitable for Greenland: MimiNet, a Tensorflow-based CNN model that runs on Ghub. In applying the MimiNet workflow to study the interannual variability in the locations and size of the crevassed areas in Pâkitsoq, central western Greenland. We found no overall trend in the crevasse extent over 2015–2024 contrasting the decreasing trend in crevassed area previously identified in the region (Chudley and others, 2025). The size and locations of crevasse fields were highly persistent over our ten-year study period, in agreement with a previous work (Hoffman and others, 2018). Throughout our study period, we identified some seasonal velocity signals with a spring speedup in June and slowdown which occurred through August and September of each year. By using flow speed anomalies as a window onto the efficiency of the subglacial drainage network, we infer that crevasse fields in Pâkitsoq deliver meltwater to the bed but while moulin-drained areas are better able to efficiently route meltwater directly to the bed and drive seasonal changes in the subglacial drainage system structure and efficiency. Our workflow enables future research to study the spatial distribution and temporal trends in crevasse fields on ice masses surveyed by the Sentinel-1 satellite constellation. We envision that the improvement of SAR-despeckling techniques will lead to highly accurate crevasse detection results. Continuous mapping of crevasses will be beneficial to study the changing ice dynamics of both slow-moving and fast-moving glaciers on the Greenland Ice Sheet.

For Peer Review

Supplementary Material

The supplementary material for this article can be found at [url].

Code and data availability

The workflow for crevasse field detection in Pâkitsoq, Greenland is available on Zenodo (https://doi.org/10.5281/zenodo.15116011) as well as accessible as a Ghub Tool (https://theghub.org/resources/crevassedetect).

Author Contributions

KP, NK and SN conceived the study. NK and KP curated the data. NK, KP, AA, and MV conducted the data analysis. KP, JB, and SN acquired the funding. NK, AA, and MV performed data collection. NK, KP, SN, JB, and JM designed the methods. KP, SN, and JB managed and coordinated the study. KP, SN, and JB provided the computing resources. NK, KP, and JM designed and implemented the code. KP, SN, JB, and JM provided supervision. NK and KP validated the research outputs. NK and KP prepared the data presentation. NK and KP prepared the original manuscript. All authors contributed to reviewing and editing the final manuscript.

For Peer Review

Acknowledgements

This work was supported by NASA award 80NSSC19K0054 (KP) and NSF award 2004302 (JB, SN, and KP). Computing resources for this work were supplied and supported by the University at Buffalo's Center for Computational Research (CCR).

Competing Interests

The authors declare no competing interests.

References

Abadi M and 21 others (2016) {TensorFlow}: a system for {Large-Scale} machine learning. In *12th USENIX symposium on operating systems design and implementation (OSDI 16)* (pp. 265-283).

Akeret J, Chang C, Lucchi A and Refregier A (2016) Radio frequency interference mitigation using deep convolutional neural networks. Retrieved from https://arxiv.org/abs/1609.09077

Alley RB, Dupont TK, Parizek BR and Anandakrishnan S (2005) Access of surface meltwater to beds of sub-freezing glaciers: preliminary insights. *Annals of Glaciology*, *40*, 8-14. https://doi.org/10.3189/172756405781813483

884 Alzubaidi L and 9 others (2021) Review of deep learning: concepts, CNN architectures, challenges,
885 applications, future directions. *Journal of Big Data*, *8*, pp.1-74.
886 https://doi.org/10.1186/s40537-021-00444-8

887 Andrews LC and 7 others (2014) Direct observations of evolving subglacial drainage beneath the
888 Greenland Ice Sheet. *Nature*, *514*(7520), 80-83. https://doi.org/10.1038/nature13796

889 Andrews LC and 8 others (2018) Seasonal evolution of the subglacial hydrologic system modified
890 by supraglacial lake drainage in western Greenland. *Journal of Geophysical Research: Earth*
891 *Surface*, *123*(6), 1479-1496. https://doi.org/10.1029/2017JF004585

892 Banwell AF, Willis IC, and Arnold NS (2013) Modeling subglacial water routing at Paakitsoq, W
893 Greenland. *Journal of Geophysical Research: Earth Surface*, *118*(3), 1282–1295.
894 https://doi.org/10.1002/jgrf.20093

895 Banwell A, Hewitt I, Willis I, and Arnold N (2016) Moulin density controls drainage development
896 beneath the Greenland ice sheet. *Journal of Geophysical Research: Earth Surface*, *121*(12),
897 2248-2269. https://doi.org/10.1002/2015JF003801

898 Bartholomew I, Nienow P, Mair D, Hubbard A, King MA and Sole A (2010). Seasonal evolution
899 of subglacial drainage and acceleration in a Greenland outlet glacier. *Nature Geoscience*,
900 *3*(6), 408-411. https://doi.org/10.1038/ngeo863

901 Baumhoer CA, Dietz AJ, Kneisel C and Kuenzer C (2019) Automated Extraction of Antarctic
902 Glacier and Ice Shelf Fronts from Sentinel-1 Imagery Using Deep Learning. *Remote*
903 *Sensing*, *11*(21), 2529. https://doi.org/10.3390/rs11212529

904 Buduma N, Buduma N and Papa J (2022) *Fundamentals of deep learning*. "O'Reilly Media, Inc.".

905 Catania GA and Neumann TA (2010) Persistent englacial drainage features in the Greenland Ice
906 Sheet. *Geophysical Research Letters*, *37*(2). https://doi.org/10.1029/2009GL041108

907 Cheng D and 6 others (2021) Calving Front Machine (CALFIN): glacial termini dataset and
908 automated deep learning extraction method for Greenland, 1972–2019. *The Cryosphere*,
909 *15*(3), 1663–1675. https://doi.org/10.5194/tc-15-1663-2021

910 Chu X, Yao X, Duan H, Chen C, Li J and Pang W (2022) Glacier extraction based on high-spatial-
911 resolution remote-sensing images using a deep-learning approach with attention
912 mechanism. *The Cryosphere*, *16*(10), 4273-4289. https://doi.org/10.5194/tc-16-4273-2022

913 Chudley TR and 7 others (2021) Controls on Water Storage and Drainage in Crevasses on the
914 Greenland Ice Sheet. *Journal of Geophysical Research: Earth Surface*, *126*(9).
915 https://doi.org/10.1029/2021jf006287

916 Chudley TR, Howat I, King M and MacKie EJ (2025) Increased crevassing across

For Peer Review

accelerating Greenland Ice Sheet margins. *Nature Geoscience*, 1-6. https://doi.org/10.1038/s41561-024-01636-6

Clark S (2023) Jupyter Lab (202210). Retrieved from https://theghub.org/resources/jupyterlab70

Colgan W and 7 others (2011) An increase in crevasse extent, West Greenland: Hydrologic implications. *Geophysical Research Letters*, *38*(18), n/a-n/a. https://doi.org/10.1029/2011gl048491

Colgan W and 6 others (2016) Glacier crevasses: Observations, models, and mass balance implications. *Reviews of Geophysics*, *54*(1), 119–161. https://doi.org/10.1002/2015rg000504

Cook JC (1956) Some observations in a northwest Greenland crevasse, *Eos Trans. AGU*, 37(6), 715–718, https://doi.org/10.1029/TR037i006p00715.

Cuffey KM and Paterson WSB (2010) *The physics of glaciers*. Academic Press.

Das SB and 6 others (2008) Fracture Propagation to the Base of the Greenland Ice Sheet During Supraglacial Lake Drainage. *Science*, *320*(5877), 778–781. https://doi.org/10.1126/science.1153360

Dow CF, Kulessa B, Rutt IC, Doyle SH and Hubbard A (2014) Upper bounds on subglacial channel development for interior regions of the Greenland ice sheet. *Journal of Glaciology*, *60*(224), 1044-1052. https://doi.org/10.3189/2014JoG14J093

Echelmeyer K, Clarke TS and Harrison WD (1991) Surficial glaciology of Jakobshavns Isbræ, West Greenland: Part I. Surface morphology. *Journal of Glaciology*, *37*(127), 368-382. https://doi.org/10.3189/S0022143000005803

Eder K, Reidler C, Mayer C and Leopold M (2008) Crevasse detection in Alpine areas using ground penetrating radar as a component for a mountain guide system. *The International Archives of the Photogrammetry, Remote Sensing and Spatial Information Sciences*, *37*, 837-841.

European Space Agency (2014) *Sentinel-1 User Handbook*, GMES-S1OP-EOPG-TN-13-0001, ESRIN, Frascati, Italy. https://sentinel.esa.int

Fitzpatrick AAW and 9 others (2014) A decade (2002–2012) of supraglacial lake volume estimates across Russell Glacier, West Greenland. *The Cryosphere*, *8*(1), 107-121. https://doi.org/10.5194/tc-8-107-2014

Flowers GE (2010) Glacier hydromechanics: early insights and the lasting legacy of three works by Iken and colleagues. *Journal of Glaciology*, *56*(200), 1069-1078. https://doi.org/10.3189/002214311796406103

For Peer Review

950 Gardner AS and 8 others (2025) ITS_LIVE global glacier velocity data in near real time.
951 *EGUsphere*, *2025*, 1-29. https://doi.org/10.5194/egusphere-2025-392

952 Gorelick N, Hancher M, Dixon M, Ilyushchenko S, Thau D and Moore R (2017) Google Earth
953 Engine: Planetary-scale geospatial analysis for everyone. *Remote Sensing of Environment*,
954 *202*, 18–27. https://doi.org/10.1016/j.rse.2017.06.031

955 Gu J and 10 others (2018) Recent advances in convolutional neural networks. *Pattern recognition*,
956 *77*, pp.354-377. https://doi.org/10.1016/j.patcog.2017.10.013

957 Gudmundsson GH (2003) Transmission of basal variability to a glacier surface. *Journal of*
958 *Geophysical Research: Solid Earth*, *108*(B5). https://doi.org/10.1029/2002JB002107

959 Gulley JD, Grabiec M, Martin JB, Jania J, Catania GA and Glowacki PS (2012) The effect of
960 discrete recharge by moulins and heterogeneity in flow-path efficiency at glacier beds on
961 subglacial hydrology. Journal of Glaciology, 58(211), 926–940.
962 https://doi.org/10.3189/2012JoG11J189

963 Herrmann O and 6 others (2023) Out-of-the-box calving front detection method using deep-
964 learning. *The Cryosphere Discussions*, *2023*, 1-24. https://doi.org/10.5194/tc-17-4957-2023

965 Herzfeld UC, Trantow T, Lawson M, Hans J and Medley G (2021) Surface heights and crevasse
966 morphologies of surging and fast-moving glaciers from ICESat-2 laser altimeter data-
967 Application of the density-dimension algorithm (DDA-ice) and evaluation using airborne
968 altimeter and Planet SkySat data. *Science of Remote Sensing*, *3*, 100013.
969 https://doi.org/10.1016/j.srs.2020.100013

970 Hoffman MJ and 7 others (2018) Widespread Moulin Formation During Supraglacial Lake
971 Drainages in Greenland. *Geophysical Research Letters*, *45*(2), 778–788.
972 https://doi.org/10.1002/2017gl075659

973 Hoffman AO and 7 others (2025) Inland migration of near-surface crevasses in the Amundsen Sea
974 Sector, West Antarctica. *The Cryosphere, 19(3),* 1353-1372. https://doi.org/10.5194/tc-19-
975 1353-2025

976 Hooke RL (1989) Englacial and subglacial hydrology: a qualitative review. *Arctic and Alpine*
977 *Research*, *21*(3), 221-233. https://doi.org/10.1080/00040851.1989.12002734

978 Howat IM, Negrete A and Smith BE (2014) The Greenland Ice Mapping Project (GIMP) land
979 classification and surface elevation datasets. *The Cryosphere*, *8*, 1509-1518.
980 https://doi.org/10.5194/tc-8-1509-2014

981 Joughin I and 9 others (2013) Influence of ice-sheet geometry and supraglacial lakes on seasonal
982 ice-flow variability. *The Cryosphere*, *7*(4), 1185-1192. https://doi.org/10.5194/tc-7-1185-
983 2013

For Peer Review

Joughin I, Shean DE, Smith BE and Floricioiu D (2020) A decade of variability on Jakobshavn Isbræ: ocean temperatures pace speed through influence on mélange rigidity. *The Cryosphere*, *14*(1), 211-227.

Kaluzienski L, Koons P, Enderlin E, Hamilton G, Courville Z and Arcone S (2019) Crevasse initiation and history within the McMurdo Shear Zone, Antarctica. *Journal of Glaciology*, *65*(254), 989-999. https://doi.org/10.1017/jog.2019.65

Khazendar A and 13 others (2019) Interruption of two decades of Jakobshavn Isbrae acceleration and thinning as regional ocean cools. *Nature Geoscience*, *12*(4), 277-283. https://doi.org/10.1038/s41561-019-0329-3

Koike K, Yoshida H, Omura M, Shibuya K and Doi K (2012) Temporal changes in crevasses in the middle Slessor Glacier, Coats Land, East Antarctica through SAR data analysis. *Earth, planets and space*, *64*, 257-267. https://doi.org/10.5047/eps.2011.10.003

Koziol C, Arnold N, Pope A and Colgan W (2017) Quantifying supraglacial meltwater pathways in the Paakitsoq region, West Greenland. *Journal of Glaciology*, *63*(239), 464–476. https://doi.org/10.1017/jog.2017.5

Koziol CP and Arnold N (2018) Modelling seasonal meltwater forcing of the velocity of land-terminating margins of the Greenland Ice Sheet. *The Cryosphere*, *12*(3), 971-991. https://doi.org/10.5194/tc-12-971-2018

Krawczynski MJ, Behn MD, Das SB and Joughin I (2009) Constraints on the lake volume required for hydro-fracture through ice sheets. *Geophysical Research Letters*, *36*(10). https://doi.org/10.1029/2008GL036765

Lai C-Y and 7 others (2020) Vulnerability of Antarctica's ice shelves to meltwater-driven fracture. *Nature*, *584*(7822), 574–578. https://doi.org/10.1038/s41586-020-2627-8

LeCun Y, Bengio Y and Hinton G (2015) Deep learning. *Nature*, *521*(7553), 436-444. https://doi.org/10.1038/nature14539

Libert L, Wuite J and Nagler T (2022) Automatic delineation of cracks with Sentinel-1 interferometry for monitoring ice shelf damage and calving. *The Cryosphere*, *16*(4), 1523-1542. https://doi.org/10.5194/tc-16-1523-2022

Loebel E and 7 others (2023) Calving front monitoring at sub-seasonal resolution: a deep learning application to Greenland glaciers. *The Cryosphere Discussions*, *2023*, 1-21. https://doi.org/10.5194/tc-18-3315-2024

Long J, Shelhamer E and Darrell T (2015) Fully convolutional networks for semantic segmentation. In *Proceedings of the IEEE conference on computer vision and pattern recognition* (pp. 3431-3440).

For Peer Review

Lüthi MP and 7 others (2015) Heat sources within the Greenland Ice Sheet: dissipation, temperate paleo-firn and cryo-hydrologic warming. *The Cryosphere*, *9*(1), 245-253. https://doi.org/10.5194/tc-9-245-2015

Marin C and 8 others (2020) Use of Sentinel-1 radar observations to evaluate snowmelt dynamics in alpine regions. *The Cryosphere*, *14*(3), 935-956. https://doi.org/10.5194/tc-14-935-2020

Marsh OJ, Price D, Courville ZR and Floricioiu D (2021) Crevasse and rift detection in Antarctica from TerraSAR-X satellite imagery. *Cold Regions Science and Technology*, *187*(103284). https://doi.org/10.1016/j.coldregions.2021.103284

Marshall E, Henderson S and Cherian D (2022) e-marshall/itslive: itslive tutorial updates (v.1.0.0). Zenodo. https://doi.org/10.5281/zenodo.6804325

McGrath D, Colgan W, Steffen K, Lauffenburger P, and Balog J (2011) Assessing the summer water budget of a moulin basin in the Sermeq Avannarleq ablation region, Greenland ice sheet. Journal of Glaciology, 57(205), 954-964. https://doi.org/10.3189/002214311798043735

Mejia JZ and 6 others (2021) Isolated cavities dominate Greenland Ice Sheet dynamic response to lake drainage. *Geophysical Research Letters*, *48*(19), e2021GL094762. https://doi.org/10.1029/2021GL094762

Mejia JZ and 7 others (2022) Moulin density controls the timing of peak pressurization within the Greenland Ice Sheet's subglacial drainage system. *Geophysical Research Letters*, *49*(22), e2022GL100058. https://doi.org/10.1029/2022GL100058

Mohajerani Y, Wood M, Velicogna I and Rignot E (2019) Detection of Glacier Calving Margins with Convolutional Neural Networks: A Case Study. *Remote Sensing*, *11*(1), 74. https://doi.org/10.3390/rs11010074

Moolayil J and Moolayil J (2019) Keras in action. *Learn Keras for Deep Neural Networks: A Fast-Track Approach to Modern Deep Learning with Python*, 17-52. https://doi.org/10.1007/978-1-4842-4240-7_2

Morlighem M and others (2022) IceBridge BedMachine Greenland (IDBMG4, Version 5) [Data Set] Boulder, Colorado USA. NASA National Snow and Ice Data Center Distributed Active Archive Center. https://doi.org/10.5067/GMEVBWFLWA7X. Date Accessed 03-11-2025.

Morriss BF and 7 others (2013) A ten-year record of supraglacial lake evolution and rapid drainage in West Greenland using an automated processing algorithm for multispectral imagery. *The Cryosphere*, *7*(6), 1869-1877. https://doi.org/10.5194/tc-7-1869-2013

Nienow PW, Sole AJ, Slater DA and Cowton TR (2017). Recent advances in our understanding of

For Peer Review

the role of meltwater in the Greenland Ice Sheet system. *Current Climate Change Reports*, *3*, 330-344. https://doi.org/10.1007/s40641-017-0083-9

Nye JF (1955) Comments on Dr. Loewe's letter and notes on crevasses. *Journal of Glaciology*, *2*(17), 512-514. https://doi.org/10.3189/S0022143000032652

Otosaka, I. N., Shepherd, A., Ivins, E. R., Schlegel, N. J., Amory, C., van den Broeke, M., ... & Wouters, B. (2022). Mass balance of the Greenland and Antarctic ice sheets from 1992 to 2020. *Earth System Science Data Discussions*, *2022*, 1-33.

Pedregosa F and 15 others (2011) Scikit-learn: Machine learning in Python. *the Journal of machine Learning research*, *12*, 2825-2830.

Phillips T, Rajaram H, Colgan W, Steffen K and Abdalati W (2013) Evaluation of cryo-hydrologic warming as an explanation for increased ice velocities in the wet snow zone, Sermeq Avannarleq, West Greenland. *Journal of Geophysical Research: Earth Surface*, *118*(3), 1241-1256. https://doi.org/10.1002/jgrf.20079

Pings CJ (1961) Temperature distribution near a crevasse. *Journal of Glaciology*, *3*(30), 985-996. https://doi.org/10.3189/S0022143000017391

Poinar K (2015) *The influence of meltwater on the thermal structure and flow of the Greenland Ice Sheet* (Doctoral dissertation)

Poinar K and Andrews LC (2020) Challenges in predicting Greenland supraglacial lake drainages at the regional scale. *The Cryosphere Discussions*, *2020*, 1-46. https://doi.org/10.5194/tc-15-1455-2021

Poinar K, Joughin I, Lenaerts JT and Van Den Broeke MR (2016) Englacial latent-heat transfer has limited influence on seaward ice flux in western Greenland. *Journal of Glaciology*, *63*(237), 1-16. https://doi.org/10.1017/jog.2016.103

Poinar K, Joughin I, Lilien D, Brucker L, Kehrl L and Nowicki S (2017) Drainage of Southeast Greenland firn aquifer water through crevasses to the bed. *Frontiers in Earth Science*, *5*, 5. https://doi.org/10.3389/feart.2017.00005

Ravanel L, Lacroix E, Le Meur E, Batoux P and Malet E (2022) Multiparameter monitoring of crevasses on an Alpine glacier to understand formation and evolution of snow bridges. *Cold Regions Science and Technology*, *203*, 103643. https://doi.org/10.1016/j.coldregions.2022.103643

Reynolds B, Nowicki S and Poinar K (2025) Comprehensive assessment of stress calculations for crevasse depths and testing with crevasse penetration as damage. *The Cryosphere*, *19*(10), 5045-5073. https://doi.org/10.5194/tc-19-5045-2025

For Peer Review

Rignot E, Echelmeyer K and Krabill W (2001) Penetration depth of interferometric synthetic-aperture radar signals in snow and ice. *Geophysical Research Letters*, *28*(18), 3501-3504. https://doi.org/10.1029/2000GL012484

Ronneberger O, Fischer P and Brox T (2015) U-Net: Convolutional Networks for Biomedical Image Segmentation. Retrieved from https://arxiv.org/abs/1505.04597

Schoof C (2010) Ice-sheet acceleration driven by melt supply variability. *Nature*, *468*(7325), 803–806. https://doi.org/10.1038/nature09618

Smith LC and 15 others (2015) Efficient meltwater drainage through supraglacial streams and rivers on the southwest Greenland ice sheet. *Proceedings of the National Academy of Sciences*, *112*(4), 1001-1006. https://doi.org/10.1073/pnas.1413024112

Sperhac JM and 9 others (2021). GHub: Building a glaciology gateway to unify a community. *Concurrency and Computation: Practice and Experience*, *33*(19), p.e6130. https://doi.org/10.1002/cpe.6130

Surawy-Stepney T, Hogg AE, Cornford SL and Hogg DC (2023) *Mapping Antarctic Crevasses and their Evolution with Deep Learning Applied to Satellite Radar Imagery*. Copernicus GmbH. Retrieved from http://dx.doi.org/10.5194/tc-2023-42

Surdu CM, Duguay CR, Brown LC and Fernández Prieto D (2014) Response of ice cover on shallow lakes of the North Slope of Alaska to contemporary climate conditions (1950–2011): radar remote-sensing and numerical modeling data analysis. *The Cryosphere*, *8*(1), 167-180. https://doi.org/10.5194/tc-8-167-2014

Taurisano A, Tronstad S, Brandt O and Kohler J (2006) On the use of ground penetrating radar for detecting and reducing crevasse-hazard in Dronning Maud Land, Antarctica. *Cold Regions Science and Technology*, *45*(3), 166-177. https://doi.org/10.1016/j.coldregions.2006.03.005

TensorFlow Developers (2023) TensorFlow (v2.15.0). Zenodo. https://doi.org/10.5281/zenodo.10126399

Terven J, Cordova-Esparza DM, Ramirez-Pedraza A, Chavez-Urbiola EA and Romero-Gonzalez JA (2024) Loss functions and Metrics in Deep Learning. *arXiv preprint arXiv:2307.02694*. https://doi.org/10.48550/arXiv.2307.02694

Thomsen HH, Olesen OB, Braithwaite RJ and Weidick A (1989) Greenland ice-margin programme, a pilot study at Pâkitsoq, north-east of Jakobshavn, central West Greenland. *Rapport Grønlands Geologiske Undersøgelse*, *145*, 50-53. https://doi.org/10.34194/rapggu.v145.8073

Thompson SS, Cook S, Kulessa B, Winberry JP, Fraser AD and Galton-Fenzi BK (2020)

For Peer Review

Comparing satellite and helicopter-based methods for observing crevasses, application in East Antarctica. *Cold Regions Science and Technology*, *178*, 103128.

Trunz C and 6 others (2023) Observed and modeled moulin heads in the Pâkitsoq region of Greenland suggest subglacial channel network effects. *The Cryosphere*, *17*(12), 5075-5094. https://doi.org/10.5194/tc-17-5075-2023

van den Broeke and 7 others (2016) On the recent contribution of the Greenland ice sheet to sea level change. *The Cryosphere*, *10*(5), 1933–1946. https://doi.org/10.5194/tc-10-1933-2016

van de Wal RSW and 10 others (2015) Self-regulation of ice flow varies across the ablation area in south-west Greenland. *The Cryosphere*, *9*(2), 603-611. https://doi.org/10.5194/tc-9-603-2015

Van Wyk de Vries M, Lea JM and Ashmore DW (2023) Crevasse density, orientation and temporal variability at Narsap Sermia, Greenland. *Journal of Glaciology*, 69(277), 1125–1137. https://doi.org/10.1017/jog.2023.3

Veci L, Lu J, Foumelis M and Engdahl M (2017) ESA's multi-mission Sentinel-1 toolbox. In *EGU General Assembly Conference Abstracts* (p. 19398).

Walker B and Ray L (2019) Multi-class crevasse detection using ground penetrating radar and feature-based machine learning. In *IGARSS 2019-2019 IEEE International Geoscience and Remote Sensing Symposium* (pp. 3578-3581). IEEE. https://doi.org/10.1109/IGARSS.2019.8899148

Wang L, Sharp M, Rivard B and Steffen K (2007) Melt season duration and ice layer formation on the Greenland ice sheet, 2000–2004. *Journal of Geophysical Research: Earth Surface*, *112*(F4). https://doi.org/10.1029/2007JF000760

Williamson AG, Banwell AF, Willis IC and Arnold NS (2018) Dual-satellite (Sentinel-2 and Landsat 8) remote sensing of supraglacial lakes in Greenland. *The Cryosphere*, *12*(9), 3045-3065. https://doi.org/10.5194/tc-12-3045-2018

Yang K and Smith LC (2013) Supraglacial streams on the Greenland Ice Sheet delineated from combined spectral–shape information in high-resolution satellite imagery. *IEEE Geoscience and Remote Sensing Letters*, *10*(4), 801-805. https://doi.org/10.1109/LGRS.2012.2224316

Zeiler MD and Fergus R (2014) Visualizing and understanding convolutional networks. In *Computer Vision–ECCV 2014: 13th European Conference, Zurich, Switzerland, September 6-12, 2014, Proceedings, Part I 13* (pp. 818-833). Springer International Publishing. https://doi.org/10.1007/978-3-319-10590-1_53

Zhang E, Liu L, Huang L and Ng KS (2021) An automated, generalized, deep-learning-based method for delineating the calving fronts of Greenland glaciers from multi-sensor remote

For Peer Review

sensing imagery. *Remote Sensing of Environment*, *254*, 112265. https://doi.org/10.1016/j.rse.2020.112265

Zhao J, Liang S, Li X, Duan Y and Liang L (2022) Detection of Surface Crevasses over Antarctic Ice Shelves Using SAR Imagery and Deep Learning Method. *Remote Sensing*, *14*(3), 487. https://doi.org/10.3390/rs14030487

Zheng W, Pritchard ME, Willis MJ and Stearns LA (2019) The possible transition from glacial surge to ice stream on Vavilov Ice Cap. *Geophysical Research Letters*, 46. https://doi.org/10.1029/2019GL084948

For Peer Review